



Politecnico
di Torino

Grenoble
phelma



EPFL

Master's Degree in Nanotechnologies for ICTs
MASTER'S DEGREE THESIS

Next generation tandem solar cells characterization by luminescence

Supervisors

Dott. Amaury DELAMARRE
Dott. Jeronimo BUENCUERPO
Prof.ssa Federica CAPPELLUTI

Candidate

Chiara MELLO

ACADEMIC YEAR 2023-2024



IPVF



Centre
DE Nanosciences
& DE Nanotechnologies

ABSTRACT.....	4
LIST OF SYMBOLS	5
1. INTRODUCTION.....	7
2. PV STATE OF THE ART.....	9
3. FUNDAMENTALS OF PV	11
3.1 BASIC DESIGN OF A SOLAR CELL	11
3.1.1 Shockley-Queisser limit.....	11
3.1.2 The p-n junction	12
3.1.3 The p-i-n junction	13
3.1.4 Current-voltage characteristics	14
3.1.5 External Quantum Efficiency (EQE).....	16
3.2 TANDEM SOLAR CELLS	17
4. LUMINESCENCE OF SOLAR CELLS	20
4.1 LUMINESCENCE EMISSION AND GENERALIZED PLANCK’S LAW	20
4.2 INFORMATION CONTAINED IN THE LUMINESCENCE	21
4.2.1 Quasi-Fermi Level Splitting	22
4.2.2 Transport efficiency.....	22
4.3 PHOTOLUMINESCENCE	25
4.4 ELECTROLUMINESCENCE	26
5. EXPERIMENTAL SETUP	28
5.1 SOLAR SIMULATOR.....	28
5.2 HYPERSPECTRAL IMAGER	29
6. EXPERIMENTS AND RESULTS	32
6.1 SINGLE JUNCTION.....	32
6.1.1 GaAs single junction	32
6.1.1.1 Dark IV curve.....	32
6.1.1.2 Quasi-Fermi level splitting.....	33
6.1.1.3 Images of Electroluminescence.....	38
6.1.1.4 Images of Transport efficiency	39
6.1.2 InGaP single junction.....	42
6.2 MULTI-JUNCTION	42
6.2.1 Setup	42
6.2.2 Dark Conditions	43
6.2.2.1 Dark IV curve of the total cell.....	43
6.2.2.2 Quasi-Fermi level splitting.....	43
6.2.2.3 Images of electroluminescence	47
6.2.2.4 Images of transport efficiency.....	48
6.2.2.5 Single subcells IV curves	51
6.2.3 Under illumination	56
7. CONCLUSIONS	67
APPENDIX.....	70
A. LAMBERT’S COSINE LAW	70
B. MEASUREMENTS ON INGaP SINGLE JUNCTION	71
B.1 Dark IV curve.....	71
B.2 Quasi-Fermi level splitting	71
B.3 Images of electroluminescence	72
B.4 Images of transport efficiency.....	73
REFERENCES.....	76

Abstract

The ongoing energy transition emphasizes the crucial role of photovoltaic technology in achieving net zero emission goals by 2050. Currently, silicon solar cells dominate the market, accounting for 90% of produced panels, with efficiency close to its theoretical limit. To surpass this limit, the next generation solar cells focus on tandem devices that combine materials with different bandgaps.

This study introduces a new method that utilizes electroluminescence and photoluminescence measures to access the parameters of the single subcells of a multi-junction with spectral and spatial resolution. Thanks to a reciprocity relation, the current transport efficiency of each subcell is also exploited, giving insights about the effects of series resistances. This approach gives good results without significant time consumption, making it easy to be reproduced and efficient.

The validity of this method is proved for each subcell in a tandem at different working points, showing that it is possible to investigate the cell behavior under real operating conditions.

List of symbols

A	Absorption probability	%
Δ_{μ}	Quasi-Fermi level splitting	eV
E_g	Energy gap	eV
EL	Electroluminescence	
EQE	External Quantum efficiency	%
f_T	Transport efficiency	%
FF	Fill Factor	%
ϕ_{bb}	Black-body emission flux	$\text{cm}^{-2}\text{sr}^{-1}\text{eV}^{-1}\text{s}^{-1}$
\hbar	Planck's constant	eVs
HI	Hyperspectral Imager	
j_{01}, j_{02}	Saturation current density for 2-diode model	Acm^{-2}
J	Current density	Acm^{-2}
k	Boltzmann's constant	eVK^{-1}
PL	Photoluminescence	
q	Elementary charge	C
STC	Standard Test Conditions	25°C, 1000 Wm^{-2}
T	Temperature	K
V_{oc}	Open circuit voltage	V

1. Introduction

Photovoltaic is playing a major role in the energy transition, and its share in electricity generation is expected to continue rising to contribute to the net zero emission goals by 2050 ^[1].

Around 90 % of the currently produced solar panels are using silicon solar cells with gradually decreasing costs and increasing efficiency. Nevertheless, this efficiency is nearing its physical limit of 29.4 %, with 26.8 % obtained in laboratory ^[2]. To overcome this limit, the next generation of solar cells will consist in tandem devices, that combine materials of different bandgaps.

Those new devices present exciting challenges: new fabrication steps, new materials, new aging mechanisms and failure modes. All these aspects call for a better understanding of their working principles, through new characterization methods and data analysis.

This work exploits the developing of a new technique based on simultaneous electrical and optical carrier injection in solar cells, with which the parameters of the single subcells can be accessed with spectral and spatial resolution. One of the benefits of this method is that it should be applicable at different working points (i.e. illumination intensity and voltage), so that the cell can be investigated in conditions close to real operation. A technique that takes advantage from a reciprocity relation is exploited to compute the current transport efficiency of each subcell.

The experiments were carried out as follows: initially, a dark IV curve measurement was performed to gain a preliminary understanding of the cell's behavior. Then, the spectrum of the cell was extracted from luminescence (electroluminescence or photoluminescence) data cubes to estimate the quasi-Fermi level splitting of the cells and comment key parameters related to the Generalized Planck law of emission. The results achieved from these measures will be also used in combination with images of electroluminescence to determine the dark IV curves of individual subcells in a multi-junction configuration. Lastly, electroluminescence images are analyzed to evaluate the cell's surface and determine its transport efficiency.

The luminescence emission will be recorded with a hyperspectral imager, which produces images of luminescence at several detection wavelengths. A sourcemeter will be also used to do simultaneous electrical measures. Complementary setups such as solar simulator and EQE will be used.

This work comprises a part of experimental work in the laboratory as well as data treatment. All the data have been treated with Matlab, with a code developed ad-hoc. A Python version of the code has also been written.

The first part of the report aims to explain in more detail the scenario in which this project takes place. Then, an introduction to the physics and key features of a solar cell is done to give an in-depth understanding of the processes that will be explained after. The last chapters explain the principles of luminescence, the methods and the setup used to measure it, and finally the results of the experiments.

Despite the purpose of the work is to test and prove the validity of these characterization techniques on tandem solar cells, also measurements on single junctions have been done and are included in the results section. Considering that there is already some literature about them, they have been used as starting point to

assess the method and understand the data analysis. Moreover, once results on single junctions are processed, it will be easy to predict the behavior of subcells in tandems. All the measurements have been taken in dark condition, and despite the work focus on both electroluminescence and photoluminescence, most of the experiments involve only electroluminescence. The last part of the report exploits the injection of light on the subcell. Unfortunately, due to issues related to the background, the results achieved still need to be discussed, but they will leave interesting open question for the future.

The single junction cells have been fabricated in the IPVF institute, while the tandems were provided by a university partner of the project. The fabrication process of the cells has not been exploited since it was not relevant to this work.

2. PV state of the art

In the context of PV modules, the market is shared between 2 technologies ^[3]:

- Crystalline silicon (multi, mono)
Borrowing knowledge from microelectronics manufacturing and benefiting from its abundance and reliability, silicon-based PV modules (i.e. made of Si wafers) currently dominate the market (90%)
- Thin film (CdTe, Perovskites)
The peculiarity of this technology is the possibility to directly deposit the material (with a thickness of only few micro-meters) on the internal surface of the glass modules. Compared to the production based on crystalline wafers, this technology involves less material usage and the possibility to be used on flexible substrates. Nevertheless, the performances in efficiency are lower compared to c-Si (except for Perovskites, which however present issues in up-scaling, stability, and toxicity).

In general, the decision for or against investment in a PV system is based on costs per Watt. Therefore, one of the biggest challenges of PV is to produce cells and modules in a more cost-effective way. One of the possibilities to do that is to increase the efficiency, which means more Watts for the same production costs. Increasing efficiency means smaller cells, which implies cost reductions due to less panels to be installed, less manufacture costs, etc...

Table 1 reproduces the record efficiency of the different PV technologies under STC (Solar cell efficiency tables version 63, 2024) ^[2].

	Lab scale cell efficiency (%)
c-Si	26.8 ± 0.4
GaAs	29.1 ± 0.6
CdTe	23.35 ± 0.5
CIGS	21.0 ± 0.4
Perovskite	25.2 ± 0.8
InGaP/GaAs/InGaAs	37.9 ± 1.2
InGaP/GaAs	32.8 ± 1.4
InGaP/GaInAsP/Si	36.1 ± 1.3
Perovskite/Si	33.9 ± 0.3

Table 1. Confirmed efficiency of the different PV technologies under STC.

Based on the results showed in Table 1, the highest conversion efficiency of all PV technologies is achieved by multi-junction cells with III-V materials. The most used design is a stack of 2 or 3 junction cells, which involve usually InGaP and GaAs as materials for the subcells.

The main drawback of these cells is the cost. Indeed, the choice of the substrate, the growth processes and manufacturing have a huge impact on the overall cost of the

production of this technology, making it expensive: high cost per tool, high cost precursors, etc..^[4].

Another possibility is to mechanically stack cells on top of c-Si. This technique is particularly convenient, because silicon has demonstrated long stability and reliability in the field, which is crucial for the commercial availability. Moreover, the results obtained are promising: this concept now reached efficiencies of 36.1 % for III-V multi-junctions and 33.9% for perovskites, as it is highlighted in the table above.

Therefore, tandem cells are expected to be the next generation of PV modules. The future market will be dominated by tandems, especially on c-Si.

3. Fundamentals of PV

To describe a solar cell, the starting point is to talk about semiconductor physics.

The basic components of a solar cell are:

- One absorber, which is the layer that absorbs sunlight to generate electron-hole pairs
- An electron transport layer (ETL), which is designed to allow only electrons to pass through while blocking holes. It is typically made of n-type material
- A hole transport layer (HTL), which is designed to allow only holes to pass through while blocking electrons. It is typically made of p-type material

In this configuration, when light is absorbed by the absorber, electron-hole pairs are generated. The electron transport layer attracts the electrons to the negative contact, while the hole transport layer does the same with holes to the positive contact, generating a current.

3.1 Basic design of a solar cell

3.1.1 Shockley-Queisser limit

In 1961, Shockley and Queisser ^[5] derived a limit for the maximum theoretical efficiency of single junction solar cells. The result of their study is based on three losses:

- Thermalization losses
Photons with energy higher than the bandgap lose their excess energy as heat, as electron relaxes back to the band edge.
- Recombination losses
All the photons with energy exceeding the bandgap are ideally absorbed. As complementary and reverse process, radiative recombination must be considered as one type of loss.
- Spectrum losses
Photons above the bandgap contribute to thermalization losses, while photons below the bandgap are entirely lost.

Based on this assumption, they stated that the maximum efficiency for a solar cell with a bandgap of 1.37 eV under AM1.5G solar spectrum is 33.7%. For the bandgap of c-Si, the limit is between 29.4 and 29.6%. Figure 1 reproduces the SQ-limit as a function of the band gap energy considering the AM1.5G spectrum.

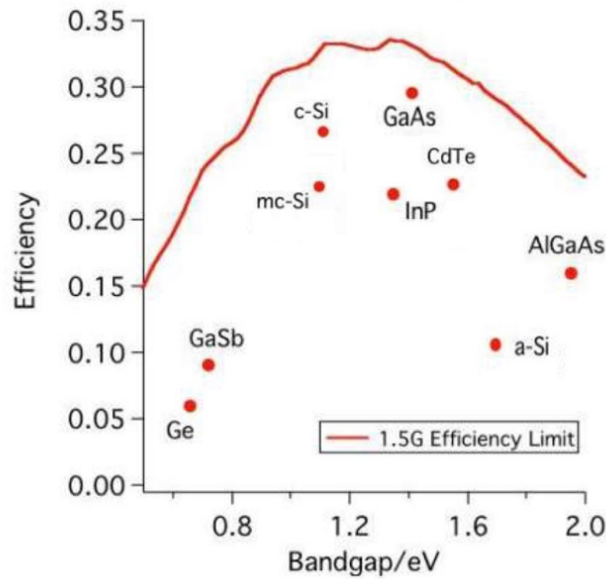


Figure 1. SQ-limit as function of the E_g for single junctions under AM1.5G. The points represent the best experimental single bandgap cells fabricated to date.

Credit of the image: <http://www.physics.usyd.edu.au/app/solar/research/pv.html>

However, there are methods for solar cells to exceed this limit, and higher efficiencies are possible. An experimentally proven way is the use of more than one junction, in a stack called “multi-junction” or “tandem”. The limit for tandem cells with two junctions is 47%, and for devices with an infinite number of stacked junction reaches 68% [6].

3.1.2 The p-n junction

A basic solar cell is designed with a p-n junction that converts the energy of light into direct current (DC) electricity using the photovoltaic (PV) effect.

A p-n junction is the combination of a p-doped and an n-doped semiconductor. Globally, the two materials are neutral, except for a region obtained at the interface of the junction (space charge region, or depleted region), where the majority carriers of each semiconductor feel a concentration gradient that drive them in the opposite region, so that they recombine and leave behind their ionized dopants. An electric field is as well generated and balances the diffusion process of the carriers. Figure 2 shows the working principle of a solar cell with a p-n junction [7].

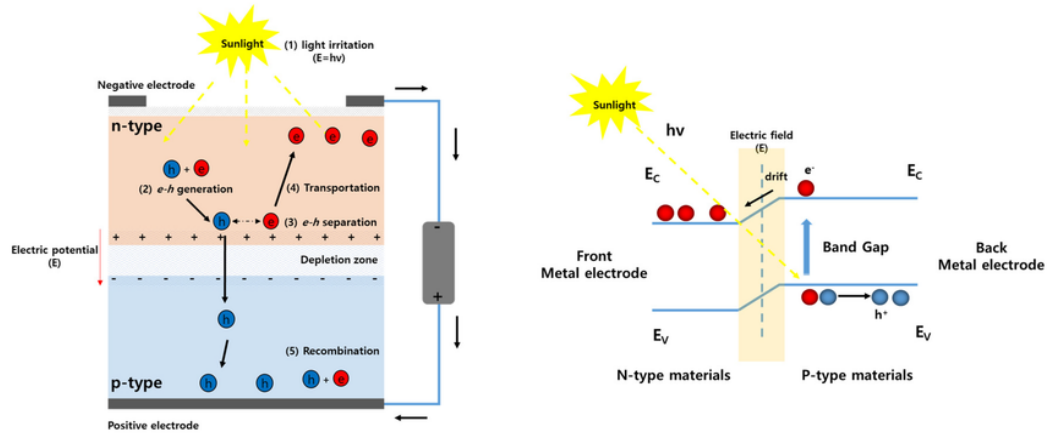


Figure 2. Working principle of a solar cell with a p-n junction. As electrons and holes are diffused to the opposite low-charge concentration of each material, the depleted region is created at the junction interface. The depletion layer is typically small, and the electric field E is present inside the depleted region without electron–hole recombination.

The process showed above goes through the following steps:

1. *Light irradiation*: photons impinge on the solar cell.
2. *Electron-hole pairs generation*: the solar cell absorbs the photons, generating e-h pairs.
- 3-4. *Electron-hole pairs separation*: the built-in voltage at the junction drives holes into the p-type layer, while the electron flow through the n-type layer, which is connected to an external load. This provides a path for electrons through the p-type material, and this movement generates electricity.
5. *Recombination*: the electrons return to the cell after exiting the external load, where they meet holes and recombine.

3.1.3 The p-i-n junction

Another common configuration is the p-i-n junction, which incorporates an intrinsic layer between the p-type and n-type materials. This intrinsic layer is made by an undoped (or slightly doped) semiconductor. It provides better separation of e-h pairs and helps to reduce recombination.

This configuration can be used with various materials, making it suitable in new PV technologies, for example perovskite solar cells [8].

Figure 3 shows the configuration of a p-i-n perovskite solar cell. The transparent conductive oxide layer allows light to pass through while providing a conductive pathway for electrons.

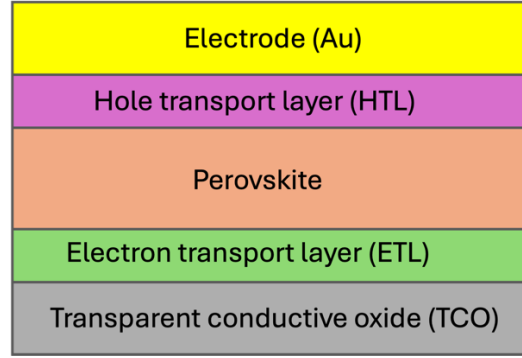


Figure 3. Schematic of a thin film perovskite solar cell.

The principle of operation is the same as for the p-n junction: the light enters from the TCO, and it is absorbed by the perovskite material, generating e-h pairs. Then electrons move to the ETL, which is in contact with the TCO, while holes move to the HTL.

3.1.4 Current-voltage characteristics

The solar cell in dark is a diode. Indeed, its I-V characteristics can be described by the diode equation:

$$J(V) = j_0 \left[\exp\left(\frac{qV}{nkT}\right) - 1 \right] \quad (1)$$

Where j_0 is the saturation current density, and n is the ideality factor. The term -1 can be usually neglected during computation, since the exponential term is $\gg 1$, except for very low voltages (below 100 mV).

When the cell is under illumination, the photogenerated current j_{ph} must be taken in consideration. In this case the superposition principle holds:

$$J(V) = J_{diode}(V) - j_{ph} \quad (2)$$

The resulting characteristic is shifted downwards by an amount j_{ph} .

Figure 4 shows the I-V curves of a solar cell in dark and under illumination.

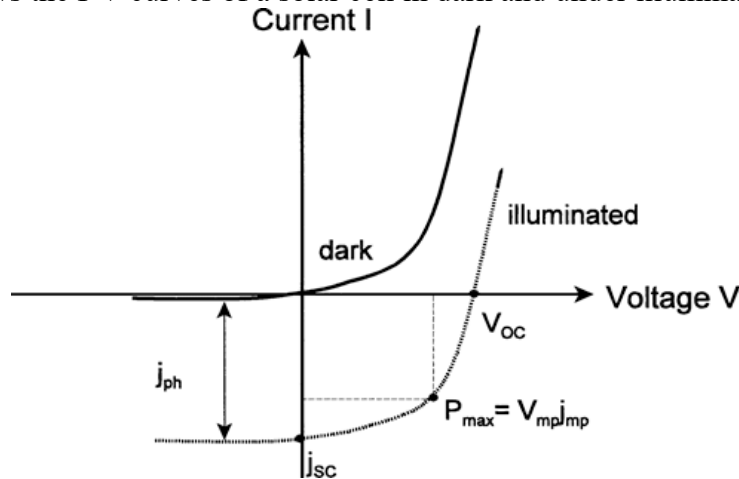


Figure 4. Current-voltage characteristics of a solar cell in dark and under illumination.

From the current-voltage characteristics above, it is possible to recognize the figures of merit of a solar cell:

- The open circuit voltage V_{oc} , which is the maximum available voltage of a solar cell, when no current is extracted from the cell (i.e. $I=0$ A)

- The short circuit current J_{sc} , which is the current that flows through the cell when no voltage is applied
- The maximum power point P_{MPP} , which is the maximum power achievable from a solar cell. It is given by the coordinates V_{MPP} and I_{MPP}

After defining these parameters, two other terms can be derived:

- The Fill Factor FF, which is defined as the ratio of the maximum power and the product of the open circuit voltage and short circuit current
- The cell efficiency, which is defined as the ratio of the maximum power and the incoming energy flux (this corresponds to the AM1.5G spectrum, which is 1000 Wm^{-2} intensity)

In reality, solar cells take into account also losses due to ohmic resistances.

Therefore, the equivalent circuit of a solar cell includes a series resistance R_s , which is a contact resistance between the semiconductor and the adjacent electrodes, and a parallel resistance (also called shunt resistance) R_p , which models the loss of carriers via possible leakage paths.

Figure 5 shows the equivalent circuit of the solar cell considering R_s and R_p and a dark IV curve in log scale where the effects of R_p and R_s parameters are shown.

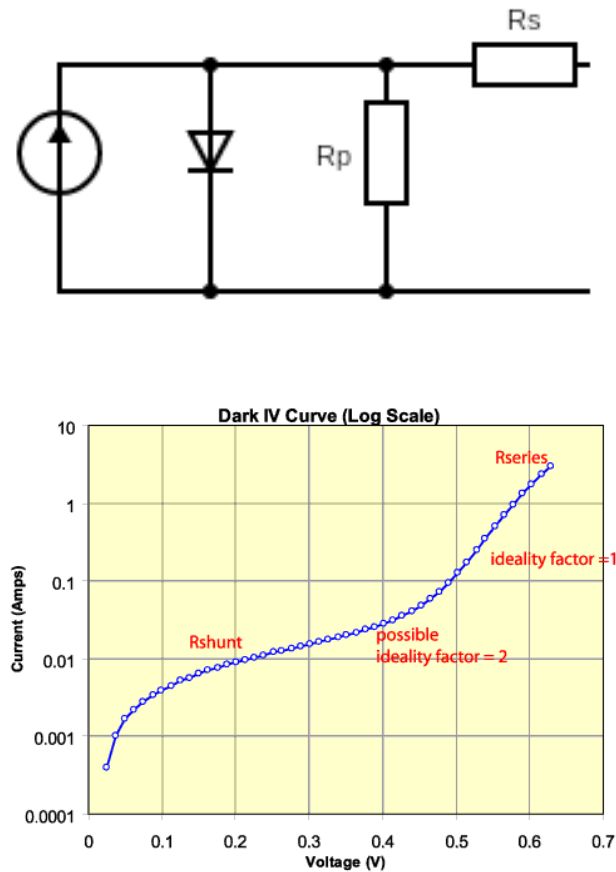


Figure 5. Equivalent one-diode model of a solar cell with R_s and R_p and dark IV curve in log scale, where the effects of R_s and R_p are highlighted.

The presence of R_s and R_p can heavily influence the I-V characteristics of a solar cell. Indeed, their behavior reflects in the two slopes of the curve. The shunt resistance affects the low-voltage range, and in presence of this effect, the curve

presents a steeper slope near I_{sc} , while the sheet resistance affects the high-voltage range, resulting in a less steep curve due to the decrease of voltage and current. In ideal conditions $R_s \sim 0$, $R_p \sim \infty$.

The single diode model assumes a constant value for the ideality factor n . In practice, the ideality factor is a function of the voltage across the device. Hence, the simple diode model is usually substituted by a 2-diode model (Figure 6).

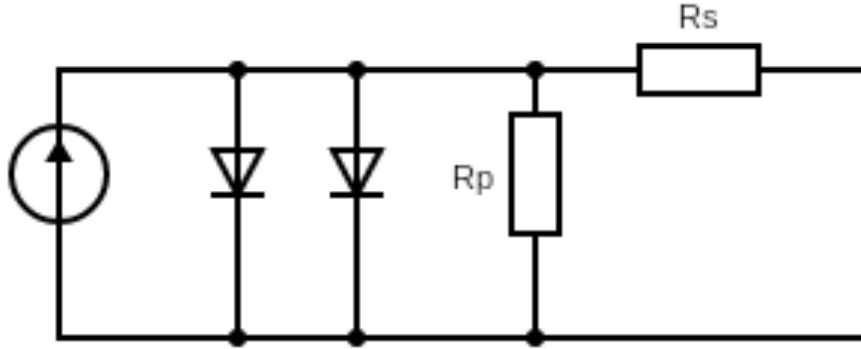


Figure 6. 2-diode model of a solar cell.

Thus, two ideality factors and two saturation current densities are considered:

- n_1 , that indicates the recombination mechanism and it is usually close to 1
- j_{01} , that depends on recombination in the quasi-neutral region
- n_2 , that indicates the defects in the space charge region, and it is usually close to 2
- j_{02} , that depends on recombination in the space charge region

3.1.5 External Quantum Efficiency (EQE)

To get further information, a representation of the spectral response can be measured. In this regard, the external quantum efficiency (EQE), defined as the ratio of collected e-h pairs over incident photons, is used to identify lossy regions within the cell. It can be determined measuring the short circuit current under a monochromatic illumination at a specific wavelength.

$$EQE = \frac{\text{\#collected } e-h \text{ pairs}}{\text{incident photons}} = \frac{J_{sc}(\lambda)/q}{P_{inc}/\hbar\omega} \quad (3)$$

A quantum efficiency curve for a silicon solar cell is shown below in Figure 7.

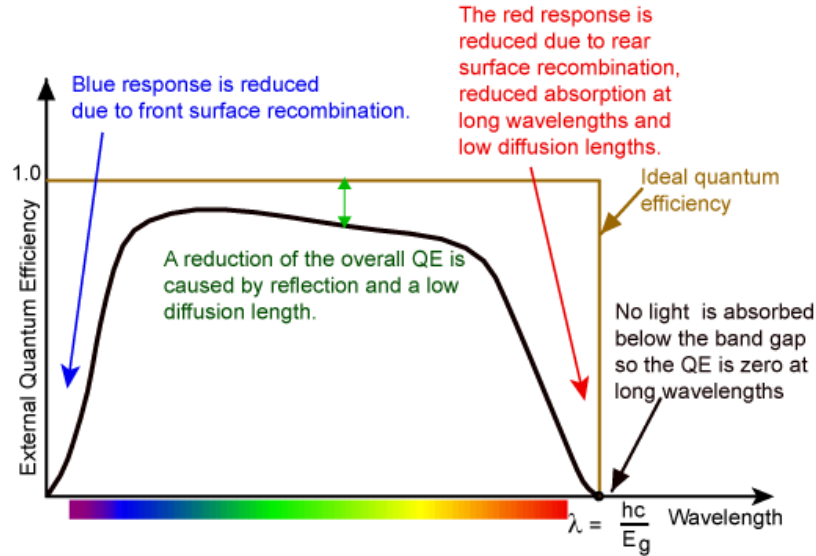


Figure 7. External Quantum Efficiency of a silicon solar cell ^[9].

Ideally, a perfect solar cell shows a quantum efficiency equal to unity, which means that all photons are absorbed, and minority carriers are collected. As said before, real solar cells suffer from recombination, which result in reduction of the EQE along the curve.

In the case showed in the figure above, low EQE in the blue region indicates parasitic absorption, while the losses in the red region are due to short diffusion length or recombination at the rear contact.

3.2 Tandem solar cells

Multi-junction solar cells, also called tandem solar cells, are a stack of p-n junctions with different band gaps. Each of them is designed to use a part of the solar spectrum. By stacking the cells in order of decreasing bandgap as shown in Figure 8, the light is automatically filtered, as each cell extract photons which exceed its bandgap. Thus, by optimizing the absorption, tandems can achieve efficiencies higher than single junction cells.

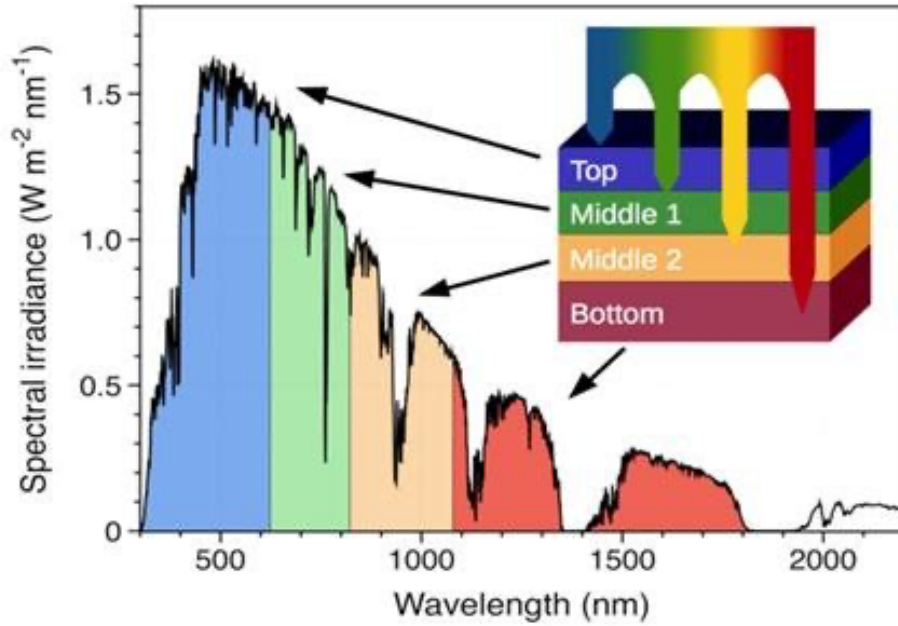


Figure 8. Spectral division in a 4 junction tandem solar cell ^[10]. The top layer has the highest E_g and absorbs the shortest wavelength photons. The process continues with decreasing band gaps until the longest wavelength photons are absorbed.

If we consider their equivalent circuit model (Figure 9), the cells are combined in series: this means that the total voltage of the junction is given by the sum of the voltages generated by each junction, and the current through the total cell is equal to the current through the junction with the lowest current density.

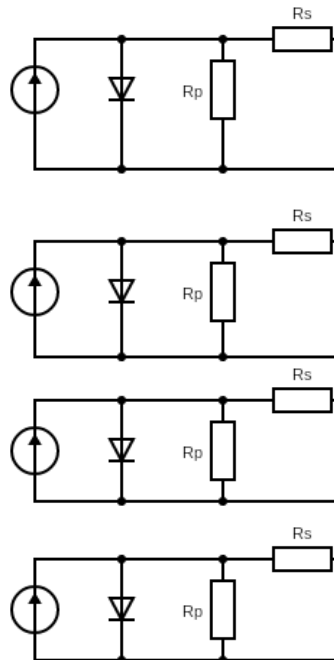


Figure 9. Equivalent electrical circuit of a 4 junction tandem solar cell.

The most used materials are III-V materials (InGaP, GaAs, Ge, GaInAs) or Perovskites due to their suitable bandgap energies and high efficiency. Despite their

promising performances, the complexity of cost, stability (in the case of perovskites), and challenges in manufacturing limit their applications.

4. Luminescence of solar cells

4.1 Luminescence emission and Generalized Planck's law

Luminescence is the emission of light from a material when photons are absorbed. When a material absorbs energy, electrons are excited from the valence band to the conduction band, creating e-h pairs. These states can then recombine and release energy in form of a photon, emitting light. This recombination phenomenon is called radiative recombination, and it is the process desired for a device to emit light. However, not all the e-h pairs that recombine result in photon emission. Indeed, there is another recombination phenomenon that might happen instead of the radiative one, called non-radiative recombination. Non-radiative recombination can occur through traps (SRH recombination) or Auger mechanisms. Figure 10 shows each of these mechanisms on a band diagram.

In radiative recombination the electron in the CB loses its energy and recombines with a hole in the VB, releasing energy in form of a photon. Defect-assisted recombination, also known as SHR recombination, involves 3 levels: CB, VB and an energy level present in the band gap called “defect state” or “trap state”, which originates from impurities present in the semiconductor lattice. Auger recombination involves 2 electrons and 1 hole: the 2 electrons in the CB collide and exchange momentum, one electron gains energy (then lost by thermalization), while the second one loses energy and falls in the VB, where it recombines with a hole.

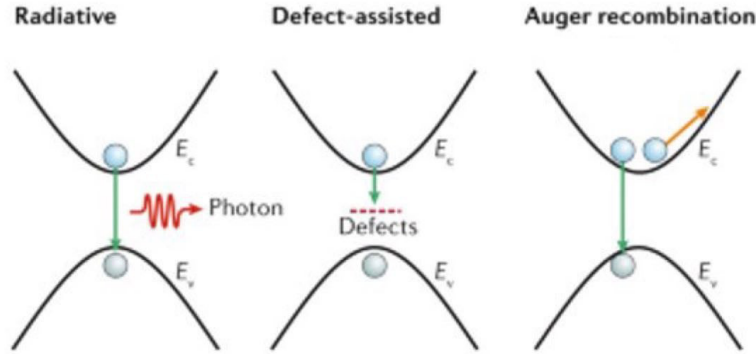


Figure 10. Recombination mechanisms occurring in a semiconductor.

The emission of light in a material produced from radiative recombination is given by a luminescence spectrum, which follows the Generalized Planck Law of emission ^[11] described by equation 4:

$$\Phi(E, r, \theta) = A(E, r, \theta) \frac{\cos \theta}{4\pi^3 \hbar^3 c_0^2} E^2 \frac{1}{\exp\left(\frac{E - \Delta\mu}{kT}\right) - 1} \quad (4)$$

Where $A(E, r, \theta)$ is the probability of absorption of an incident photon of energy E , at surface position r and angle θ , and $\Delta\mu$ is the quasi-Fermi level splitting, which is assumed to be constant in the material. Indeed, if the carrier concentration in the active region of the cell is uniform under illumination, then the qfls can be assumed constant in the depth of the cell and equal to the local diode voltage $V(x, y)$, so that $\Delta\mu \approx qV$.

The term $\cos\theta$ indicates that the emission follows the Lambert law, which is explained in the Appendix. Other constants have their usual meaning. Introducing the black body radiation flux

$$\phi_{bb}(E) = \frac{E^2}{4\pi^3 \hbar^3 c_0^2} \frac{1}{\exp\left(\frac{E}{kT}\right) - 1} \quad (5)$$

and using the Boltzmann approximation $E - qV \gg kT$, we can rewrite the emission:

$$\Phi(E, r, \theta) = A(E, r, \theta) \phi_{bb}(E) \exp\left(\frac{qV(x, y)}{kT}\right) \quad (6)$$

Moreover, a reciprocity relation^[12] states that the absorptivity at a given wavelength can be related to the external quantum efficiency at the same wavelength. This comes from the following statements:

- When light is absorbed by a material, e-h pairs are generated. The absorptivity represents the fraction of light absorbed by the material, and therefore it determines the number of e-h pairs generated
- Not all the e-h pairs generated contribute to the current; the collection efficiency dictates how many of these pairs are successfully collected and contribute to the output
- The radiative recombination, which results in the emission, is the inverse process of absorption. Therefore, the emission is directly proportional to the absorptivity

Because the EQE is determined by a product of the absorptivity and the collection efficiency of the generated carriers, with the assumptions above, it is possible to use the approximation $A f_c = \text{EQE}$. Therefore, using an approximation and considering f_c close to 1, the EQE can be used as a direct measure of the material's absorptivity.

The exact derivation needs more details, such as integration in the depth (or volume) of the cell. This is why we can use the EQE instead of A when we deal with luminescence. In general, this assumption is valid only in the case of electroluminescence and not for photoluminescence emission. But since the EQE is easier to measure than A , the approximation will be used also for the photoluminescence.

4.2 Information contained in the luminescence

The luminescence emission provides information about the characteristic of the cell. The Generalized Planck law states that the emission intensity and spectrum depend on quasi-Fermi level splitting profile, absorptivity, and temperature. Therefore, using equation 6 and the luminescence spectrum, these contributions can be determined. Moreover, the luminescence can be recorded also with a spatial resolution. Therefore, mapping of the above properties can be recorded, so that characteristics of the device are determined. Table 2 summarizes the properties that can be accessed through the characteristic of the signal.

Luminescence features	Properties that can be determined
Absolute intensity	Quasi-Fermi level characteristics
Spectrum	Assessment of the quality of the qfls, temperature determination
Images	Series resistances, shunt resistances, spatial collection efficiency, carrier lifetime

Table 2. Luminescence features and properties that can be determined through them.

In this work, particular attention has been dedicated to the evaluation of quasi-Fermi level splitting through the spectrum and computation of transport efficiency through the images.

4.2.1 Quasi-Fermi Level Splitting

The absorption of light or carrier injection process in the semiconductor creates a situation of non-equilibrium of charge carriers within the semiconductor. Therefore, the material cannot be described anymore by a single Fermi level. Eventually, electron and holes reach states close to the band edges.

This allows us to define two different Fermi levels (quasi-Fermi levels) E_{Fn} and E_{Fp} for the two carrier's populations, which indicate the chemical potentials of electrons and holes in the non-equilibrium state.

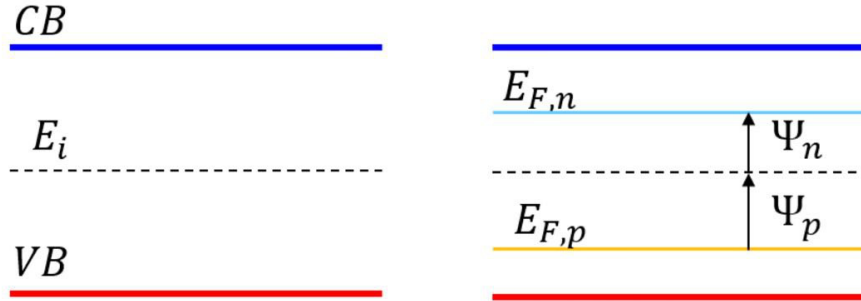


Figure 11. Illustration of intrinsic Fermi level in a semiconductor (left) and qfls under non-equilibrium conditions (right).

4.2.2 Transport efficiency

The electronic and optoelectronic reciprocity relations for solar cells can be used to highlight the effects of series resistance within the cell. In this regard, the evaluation of the current transport efficiency over the surface (x, y) of the cell can be discussed. The local transport efficiency $f_t(x, y)$ (also called collection efficiency f_c) represents the collection loss on the carrier path from the junction to the external circuit, and it is given by definition

$$f_t(x, y) = \frac{\partial i_T}{\partial i_L(x, y)} \bigg|_{\partial V_T=0} \quad (7)$$

Where i_T is the current at the terminal, while $i_L(x, y)$ is the local light-induced current collected at the junction. This value varies between 0 (no current generated is

reaching the terminal) and 1(all the current generated by light is reaching the terminal).

A reciprocity relation proposed by Wong and Green ^[13] states that

$$f_t(x, y) = \frac{\partial i_T}{\partial i_L(x, y)} \big|_{\partial V_T=0} = \frac{\partial V(x, y)}{\partial V_T} \big|_{\partial V_{i_L}=0} \quad (8)$$

where $V(x, y)$ is the local diode voltage and V_T is the voltage at the terminal. This equation can be explained with the electrical network showed for a 3J solar cell in Figure 12^[15].

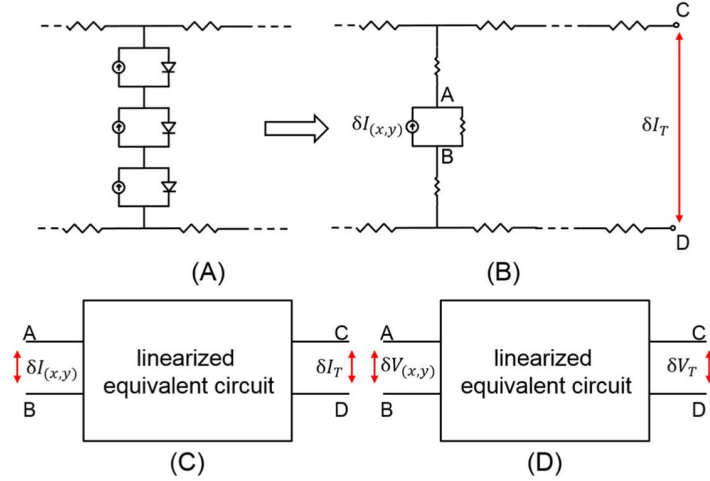


Figure 12. A, equivalent circuit of a 3J solar cell. B, equivalent circuit of the 3J cell when only a small variation of the IV curve is considered, so that all the diodes can be replaced by resistors. A small change of light source of the investigated subcell becomes the only current source in the circuit.

Since to measure f_T only a small variation of voltage or current is needed, the diodes can be replaced by resistors. Node (A,B) measures the current variation at (x,y), while node (C,D) measures the current variation at the terminal. The current efficiency is then equal to the ratio of the two. The circuit can be simplified thanks to basic circuit analysis, and as for the Lorentz reciprocity theorem

$$\frac{I_{CD}}{I_{AB}} = \frac{V_{AB}}{V_{CD}} \quad (9)$$

the current related expression for f_T can be expressed also as a function of the voltage. Moreover, the reciprocity relation still works for tandems.

Luminescence measurements can be used to compute the transport efficiency. Indeed, assuming that the qfls is constant in the depth of the cell and equal to the local diode voltage $V(x, y)$, the latter can be re-written as a function of the luminescence emission, so that equation 8 becomes

$$f_t(x, y) = \frac{\partial i_T}{\partial i_L(x, y)} \big|_{\partial V_T=0} = \frac{\partial V(x, y)}{\partial V_T} \big|_{\partial V_{i_L}=0} = \frac{\delta \ln(\phi_{em}(x, y))}{q \delta V_T / kT} \quad (10)$$

Thus, it is possible to compute f_T from luminescence images. Two images at slightly different bias voltages (the voltage variation chosen for this computation and proved to give reliable results is 10 mV) are taken.

Figure 13 shows how the map of the transport efficiency is obtained from two luminescence images of a GaAs single junction solar cell under 28 suns illumination ^[14]. The first image is taken at $V=0.90$ V, while the second one at $V=0.91$ V (10 mV step). Applying the formula discussed above, the map of the transport efficiency can be obtained.

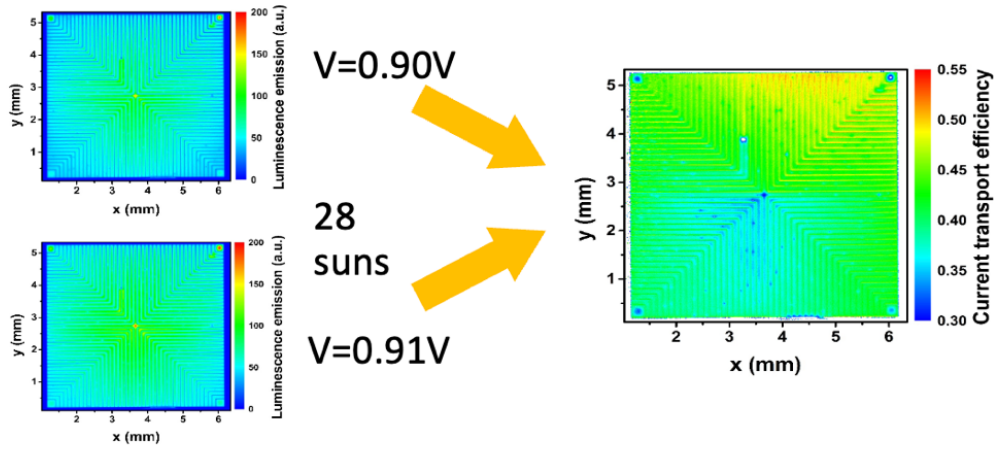


Figure 13. Example of measure of transport efficiency of a GaAs single junction cell reproduced from [14]. The cell is illuminated with an intensity of 28 suns. Two images of electroluminescence are taken, the first one at $V=0.90$ V and the second at 0.91 V. Then, applying the formula discussed above, the map of the current transport efficiency is obtained.

This method gives not only a map of the transport efficiency, but measuring different points it is also possible to reconstruct a map of the variation of the average f_T over the cell area with the voltage.

The validity of this relation has been showed experimentally in literature [14,15]. It has been compared with electrical measurements and simulations, showing a good agreement of the results (Figure 14 and 15).

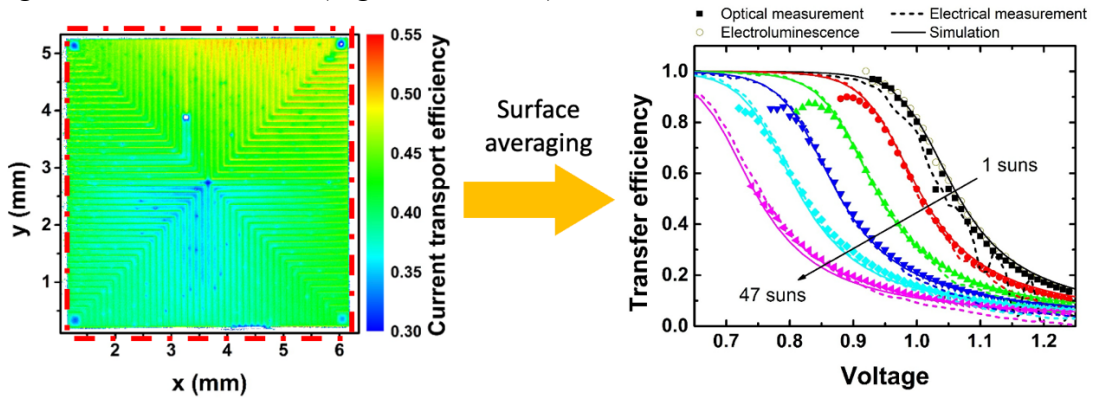


Figure 14. Averaged current transport efficiency of the GaAs single junction cell reproduced from [14] over the area of the cell under different applied voltages and illuminations obtained with 3 different methods: differential imaging (symbols), electrical measurements (dashed lines) and simulations (solid lines).

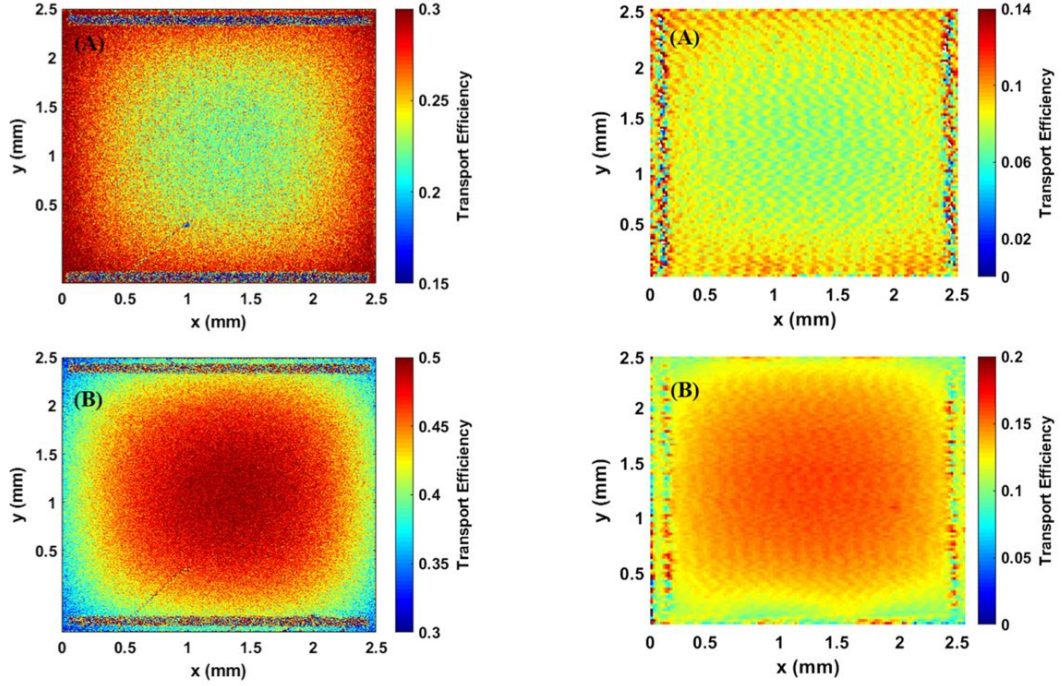


Figure 15. (Left) Maps of transport efficiency of top (A) and middle (B) subcell in a multi-junction configuration at $V=2.85$ V under illumination measured by luminescence. (Right) Maps of transport efficiency of the same cells (A is the top subcell, B is the middle one) in the same configuration measured by LBIC. The results have been reproduced from [15].

In conclusion, this method gives results with a good resolution without significant time consumption (taking an image of electroluminescence requires less than a minute; then, a Matlab code can be used to elaborate results).

4.3 Photoluminescence

Photoluminescence (PL) is the emission of light by a material resulting from a non-equilibrium state by irradiation with light. It is based on 3 processes:

1. *Excitation*: an external photon with energy higher than the energy bandgap of the semiconductor excites an electron to transit from its initially occupied valence-band state to an empty conduction-band state, generating an electron-hole pair
2. *Relaxation*: the photogenerated electron and hole from the excitation process are in general in excited states in the conduction and valence bands. They go through various energy relaxation processes to relax to their respective ground states
3. *Radiative recombination*: the electron at the conduction-bandedge state transits to the empty valence-bandedge state, where it recombines with the hole and radiatively emits a photon with a certain energy

Figure 16 shows the principle of photoluminescence with the various processes.

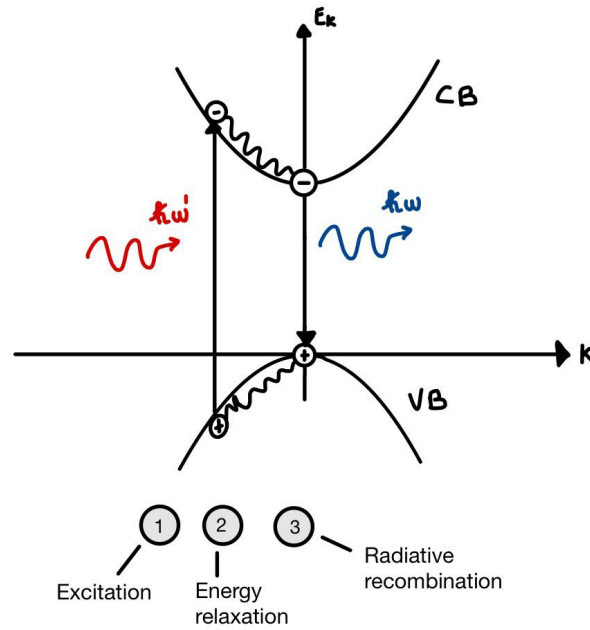


Figure 16. Schematic of photoluminescence principle in a semiconductor. A photon impinges the sample and excites an electron to transit from VB to CB (process 1); the excited electron and hole relax to their respective ground states (process 2); the electron and hole recombine radiatively to emit a photon (process 3).

In the case of a solar cell, both LED and laser excitation are valid for PL measurements. The wavelength of the excitation source is chosen properly to satisfy the condition that only photons with an energy higher than the bandgap can be absorbed.

The measure of photoluminescence is taken at open circuit conditions, to don't have influence of external electrical factors. Moreover, since there is no need of electrical contacts, the PL measurements can be done at each step of the fabrication, which makes the fabrication process easy to follow.

Thanks to spectral and spatial information, many properties of the cell can be determined:

- From the spectrum, the bandgap of the material and the quasi-Fermi level splitting are accessible; in particular, since we assumed $\Delta\mu \approx qV$, the open circuit voltage of the cell is accessible with PL, which gives an assessment of the quality of the cell. Alternatively, if the qfls is a known quantity, estimations about the other terms that can vary in the Generalized Planck law such as the temperature and the absorptivity at a given wavelength can be done
- From spatial mapping, the presence of defects and details about the lifetime can be exploited

4.4 Electroluminescence

Electroluminescence (EL) is the emission of light by a material in response to the application of a current or an electric field. The principle is the same as photoluminescence, what changes is the excitation source; in this case, a forward bias applied on the device injects carriers (electrons and holes) into it.

The voltage to apply should be generally close to the open circuit voltage to detect some luminescence, and it can be increased up to a limit value, which is chosen to be slightly above the V_{oc} in order to not damage the cell.

To measure EL both front and back contact on the cells are needed, so it can't be used at each step of the fabrication process. Nevertheless, also in this case it can be took advantage from both spectral and spatial information to determine some properties of the cell:

- From the spectrum, information about the band gap and qfls can be determined, which give information about the potential applied to the cell. Taking advantage of this feature, the IV curve of the solar cell can be also reconstructed; this is particularly interesting for the case of tandem cells, in which it possible to extract the single subcells IV curves from the total cell measurements (this will be explained later). Moreover, if the value of the qfls is known, estimations about the temperature dependence can be done.
- From spatial mapping, the effects of series and shunt resistances and insights about the collection efficiency mechanisms can be exploited.

5. Experimental setup

5.1 Solar simulator

Before estimating some parameters, a good habit is to take an IV curve, to have an idea of the behavior of the cell as a function of the voltage variation. In particular, a dark IV curve has been measured first. Measuring the curve in dark conditions is a fundamental step: knowing that a solar cell can be modeled as a diode, a dark IV characteristics helps to extract and understand the parameters of a diode such as saturation current density and ideality factor. Moreover, a dark IV curve helps in identifying non ideality factors such as high series resistance or low shunt resistance, which can indicate respectively poor interconnections or leakage paths within the cell.

Also, IV curves under illumination are exploited. Through these, the figures of merit of the cell discussed above can be easily extracted.

To perform these measurements, a solar simulator is used. A solar simulator is a device that reproduces sunlight in a laboratory setting, with special air mass filters and lamps to simulate similar intensity and spectral compositions of the sun Solar's spectrum.

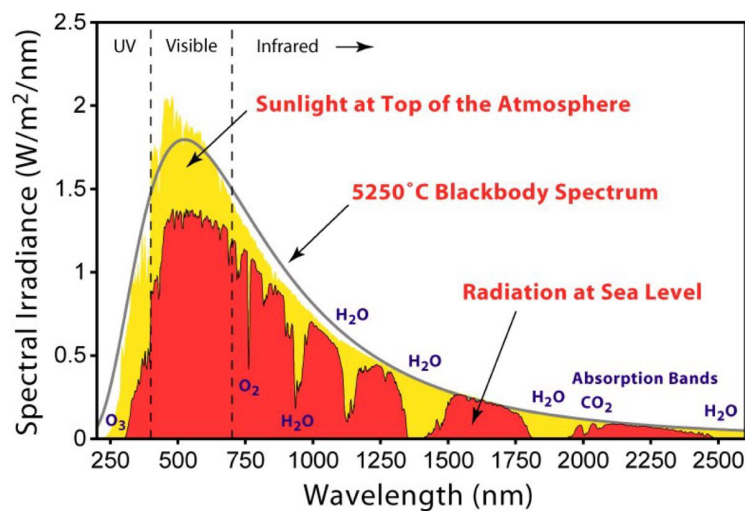


Figure 17. Characteristics of the black body radiation, solar spectrum measured in earth orbit(yellow) and on the surface of the earth(red). The mean solar irradiance is 1366 W/m^2 in outer space, and the spectrum is referred to as AM_0 . When the solar spectrum crosses the earth atmosphere it suffers from absorption and scattering phenomena.

Credit of the image: Wikimedia commons https://en.m.wikipedia.org/wiki/File:Solar_Spectrum.png

Figure 17 shows the standardized spectral illumination intensities for the cases of AM_0 and $\text{AM}_{1.5\text{G}}$. In the former, the integrated power density is 1366 Wm^{-2} , in the latter is 1000 Wm^{-2} . The reduction of the irradiance in the atmosphere is due to absorption (water vapour, dust, ozone...) and scattering (diffusion) phenomena. Solar cells are measured under standard test conditions (STC): incident spectrum of $\text{AM}_{1.5\text{G}}$ with an intensity of 1000 Wm^{-2} , equivalent to 1 sun illumination, and assumed device temperature of 25°C .

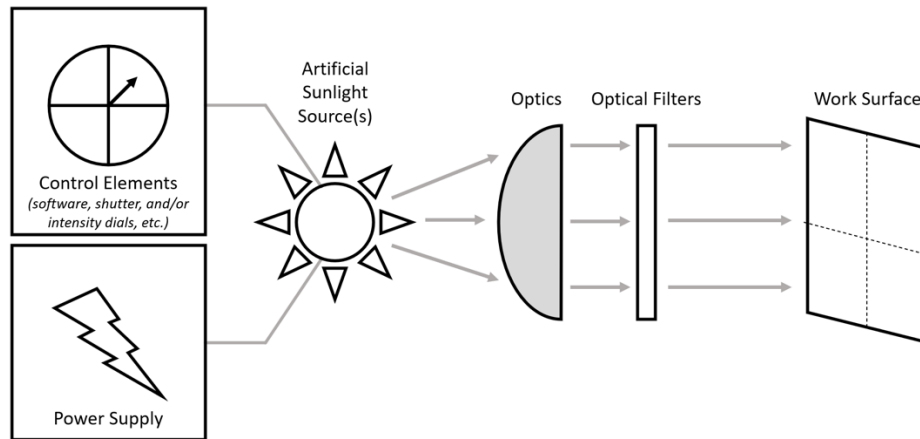
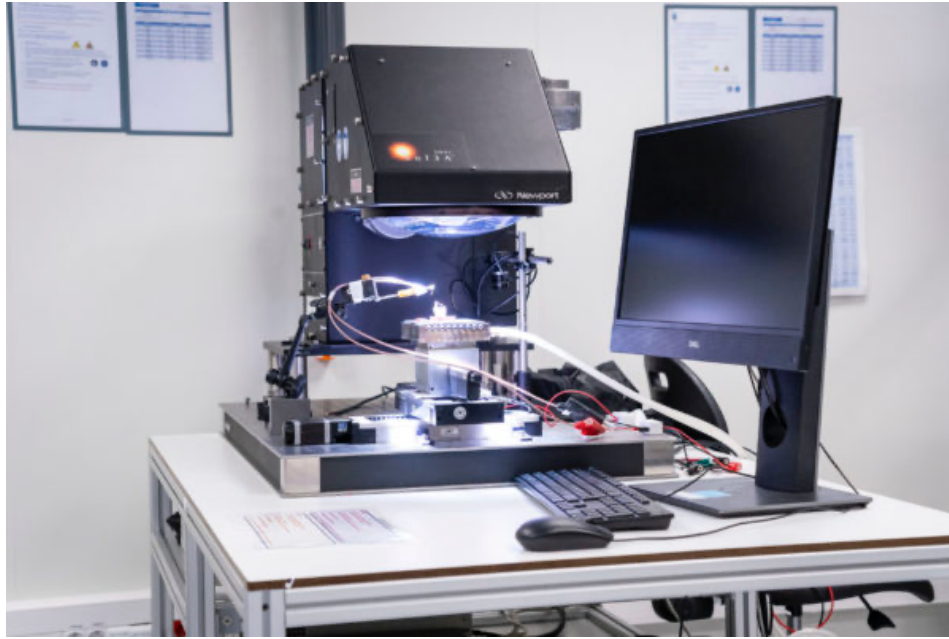


Figure 18. Solar simulator used in the lab and block scheme that shows the components of a solar simulator. The solar simulator is connected to a sourcemeter and a computer.
Credit of the images: IPVF <https://www.ipvf.fr/machines/solar-simulator-orient/>

Figure 18 shows one of the solar simulators present in the laboratory (Oriol). The cell is placed under the lamp and then electrically connected through probes. Then, a software on the computer is used to setup the data and monitor the results. To take IV curves in dark conditions a solar simulator is not necessary since there is no need of illumination. In this regard, after having contacted the cell properly, a software to measure IV curve and a sourcemeter are enough.

5.2 Hyperspectral imager

For the acquisition of luminescence, various systems are available. During this work, a hyperspectral imager (HI) has been used, which is an instrument able to record spectral and spatial properties in one acquisition. Figure 19 shows a picture of the setup and its block scheme.

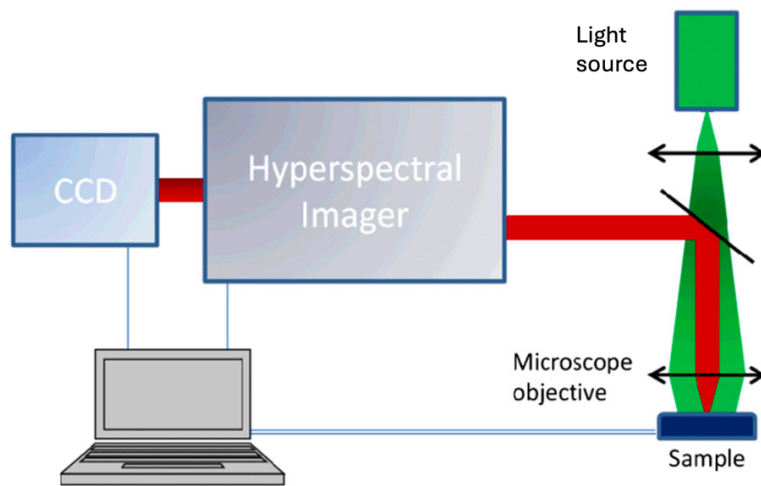
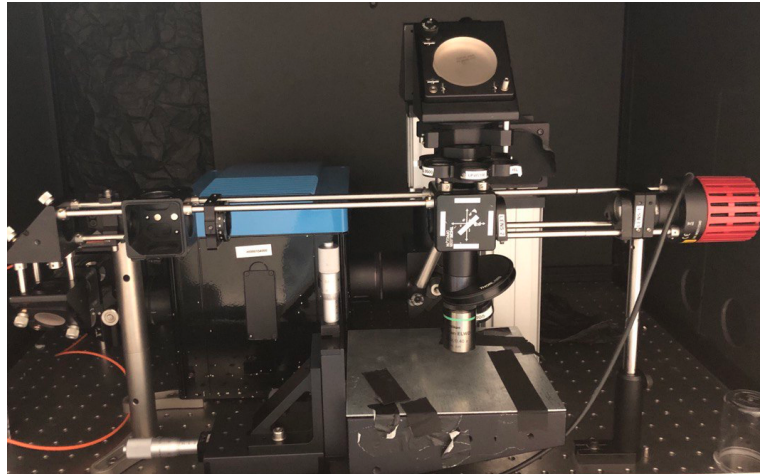


Figure 19. Hyperspectral imager setup used to measure luminescence. At the top, there is a picture of the setup taken in the lab, where several tools can be distinguished, including the light source (a LED in this case) that can be turned on, the beam splitter, and the objective. A block diagram of the setup is also provided.

The sample is illuminated by a light source (LED or laser, depending on the experiment) through a microscope objective. Then the luminescence is collected by the same objective and reflected by a beam splitter towards the detection system. The image is formed by gratings and recorded by a CCD camera.

The system can be used with a sourcemeter to take simultaneous electrical measurements. In this work, a Keithley 2536B has been used.

A software on a computer connected to the instrument is used to manipulate setup. A thermometer that indicates the temperature of the room is also available next to the setup and it will be used as indicator of temperature for the measurements.

Light sources, lenses, beam splitter, filters, objective can be changed depending on the cell and the measurements. The configuration of the setup used for the measures done in the next chapters is the following one:

- The objective used is a Nikon 40x, with a working distance of 0.19 mm
- Cube beam splitter 425 nm to deviate the light source
- LED M405LP1 as light source

- 2 collimating lenses in front of the LED
- All the measurements have been taken with the light of the room switched off

The output of the hyperspectral measurements can be 2D images containing spatial information or 3D cubes, that also contain information about the wavelength. This output is affected by an offset, which is represented by noise coming from thermal fluctuations around the setup. This offset can be corrected thanks to a dark subtraction: basically, a dark image is taken and then it is subtracted to the cube or the image measured. However, random noise cannot be completely removed, and it is one of the limits of this kind of measurements.

Another parameter to deal with during measurements is the exposure time. This parameter can be tuned through the software connected with the HI, and it must be chosen to have a signal that is high enough to get rid of the noise of the camera, but not too high to avoid saturation of the camera pixels. To correct images and cubes, after dark subtraction, they must be also divided by the exposure time.

In case of cubes, the data contained in them are measured in counts, i.e. the number of electrons contained in each pixel. Nevertheless, the unity that we use to measure the spectrum is in $\text{photons m}^{-2} \text{s}^{-1} \text{m}^{-1}$. On this purpose, a calibration procedure is performed.

The first step to perform calibration is to measure a lamp of known spectrum. This reference spectrum must be known in SI units. The lamp used for the calibration in this work is the Bentham lamp calibrated in $\text{photons m}^{-2} \text{s}^{-1} \text{nm}^{-1} \text{sr}^{-1}$ over a range from 300 nm to 1700 nm. The unit of measure of the spectrum is changed according to the unit of the measure that we want, that is $\text{photons m}^{-2} \text{s}^{-1} \text{m}^{-1}$.

The acquisition of this lamp is called “transmission cube”. Therefore, the response of the setup can be computed as

$$\text{Sensitivity}(x, y, \lambda) = \frac{\text{Transmission cube}(x, y, \lambda)}{\text{Reference spectrum}(x, y, \lambda)} \quad (11)$$

Then, after we measure a cube, the correction can be done dividing by the sensitivity

$$\text{Corrected cube}(x, y, \lambda) = \frac{\text{Measured cube}(x, y, \lambda)}{\text{Sensitivity}(x, y, \lambda)} \quad (12)$$

After the calibration of the spectrum, the configuration should be the same.

6. Experiments and results

This chapter presents the results obtained from measuring electroluminescence and photoluminescence in single junctions and tandem cells. The experiments were conducted as follows: the first step involves the dark IV curve measurement, which provides an initial understanding of the cell's behavior. Next, electroluminescence and photoluminescence spectra are extracted from luminescence data cubes to estimate the quasi-Fermi level splitting of the cells. Estimating the quasi-Fermi level splitting not only provides insights into the voltage (applied voltage for electroluminescence, and open-circuit voltage for photoluminescence) and the parameters involved in the Generalized Planck law such as Temperature and Absorptivity, but it is also used in multi-junctions to determine the dark IV curves of individual subcells. Finally, electroluminescence images will be analyzed to assess the cell's surface and derive its transport efficiency.

Most all the measurements have been taken in dark conditions. The last set chapter will also exploit the injection of light while measuring transport efficiency. Nevertheless, issues related to background had to be solved before completing the measurements. Because of this, the results are not complete, and more measurements are needed to have a complete overview. However, this will leave a good starting point for further experiments.

6.1 Single junction

Before starting to measure luminescence on a tandem solar cell, single junctions have been exploited. Working on a single junction before will allow to have a better comprehension of the results that will be shown later, because the analysis of a single junction is easier to understand, and it will give an idea of what to expect.

6.1.1 GaAs single junction

The first single junction cell exploited is a GaAs solar cell. Electroluminescence measurements on this material have been already discussed in literature ^[14,16] as GaAs single junctions are a well-known model, so measure it is a good starting point as comparisons can be done.

As said before, several parameters can be investigated from luminescence features; for these experiments, the focus will be on the quasi-Fermi level splitting and the transport efficiency.

6.1.1.1 Dark IV curve

Figure 20 shows the dark IV curve extracted for the cell. For this measure, the initial and final voltage step are set respectively to -0.5 V and 1.2 V, with a step of 0.01 V. The upper limit for the voltage is set accordingly to the bandgap of the material. A good practice is to don't exceed the value of the bandgap, but choose a value which is slightly lower, to don't damage the cell. In the case of GaAs, its bandgap is 1.42 eV, so the choice of 1.2 V is appropriate.

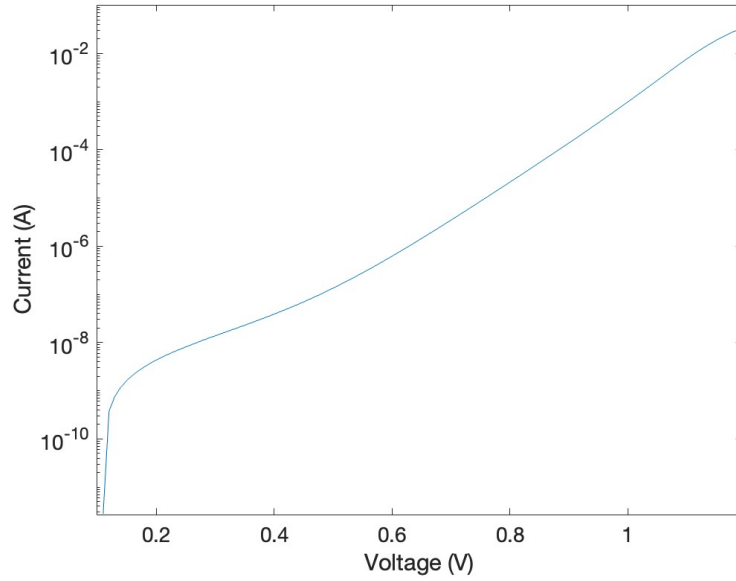


Figure 20. Plot of the dark IV curve. In the low voltage region, a deviation from the linearity indicates a high shunt resistance. At higher voltage is also possible to observe a low effect of series resistances.

As it is possible to observe from the curve, the cell works well, because at low voltages the shunt resistance is high, and at higher voltages the effects of series resistance start to appear at around 1.2 V, so it doesn't have a huge impact on the working range that will be analyzed.

This curve gives an idea of the performance of the cell under the working conditions that will be exploited in the next measurements. Since there is no significant impact of shunt resistances and the effect of series resistance is above 1 V, we expect optimal performances of the cell in the analyzed range.

6.1.1.2 Quasi-Fermi level splitting

As previously described, knowing the luminescence spectra it is possible to evaluate the quasi-Fermi level splitting $\Delta\mu$. Indeed, according to the Generalized Planck law, the absolute photon flux emitted from a semiconductor under illumination can be related to the carrier temperature and the qfls, assuming the latter is constant.

For this evaluation both PL and EL spectra have been measured, and the results will be compared.

The evaluation of the quasi-Fermi level splitting is shown to be equal to the voltage applied to the junction, in the case of electroluminescence. In a solar cell with good transport properties (long diffusion length, no potential barrier on current flow), the quasi-Fermi levels are equal to the V_{oc} for photoluminescence. Therefore, in PL we access the V_{oc} , that describes the quality of the cell.

The EL spectrum has been measured at $V=1$ V, while the PL one at open circuit conditions, with a light intensity so that $V_{oc}=1$ V. Figure 21 shows the two spectra. The unit of measure of the intensity is $\text{photons}\cdot\text{m}^{-2}\cdot\text{s}^{-1}$ and it's given by an absolute calibration performed with a Bentham lamp.

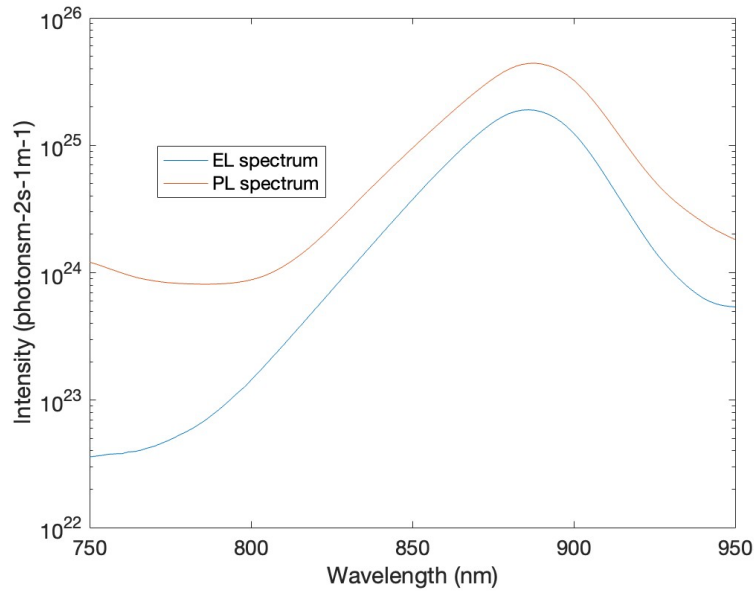


Figure 21. Electroluminescence and photoluminescence spectra. The two spectra are the results of an average over a portion of the area of the cube measured. An absolute calibration has been done with the Bentham lamp.

As it is noticeable from the figures above, the intensity peak of the spectrum indicates the material under examination. Indeed, from the wavelength that corresponds to the energy peak, it is possible to deduce a value which is close to the bandgap of the material. It is also possible to observe that the tails of the spectrum don't go to zero as they should. This is probably because the resulting intensity graph is taken as average over a portion of the cube measured, so the averaging computation, together with the calibration, can lead to this kind of issues. Moreover, the background is still an open question on this experimental setup. It probably comes from the illumination system, since on the EL spectrum it is less evident.

Once the spectrum is computed, the Generalized Planck Law can be used to estimate the quasi-Fermi level splitting.

Indeed, as explained above, the Generalized Planck Law determines the intensity of the emission, and it is connected to absorptivity, temperature, and quasi-Fermi level splitting. This means that knowing the absorptivity and the temperature, the quasi-Fermi level splitting can be evaluated. And vice-versa, having an estimation of the quasi-Fermi level splitting allows to play with the other parameters.

At first, in order to evaluate the quasi-Fermi level splitting, some assumptions are done:

- The absorptivity can be estimated, knowing the refraction at the air/material interface. Indeed, the cell does not have anti-reflection coating and back reflector, which means that we can use the refractive index of the semiconductor and then the relation $A=1-R$. The EQE is a better quantity to use, and it can be substituted to A doing an approximation.
- The temperature used in the computation is the one measured in the lab at the beginning of the measurements; however, it must be considered that this value may not be entirely accurate because the cell tends to heat up during the

measurements. Since this parameter affects the slope of the curve, adjustments will be made to achieve the best fit

- The quasi-Fermi level splitting is not depth dependent, but it is constant through the cell

Making these assumptions, the Generalized Planck Law curve can be plotted with the spectrum; the value of the quasi-Fermi level splitting is set equal to the voltage applied to measure the spectrum in the case of electroluminescence, or equal to the open circuit voltage, in the case of photoluminescence. In the best case, if all the assumptions are correct, the curve of the law should fit with the spectrum. If this is not the case, then the value of the quasi-Fermi level splitting is adjusted until the fit is found. The final value will determine the quasi-Fermi level splitting. It is possible that the values (the one used in the measurements and the one found to determine the fit) don't coincide, but usually they are close, with a discrepancy of typically between 20 meV and 40 meV [17,18].

An initial fit will be determined by setting the absorptivity value, estimated from the material's refractive index, and using the temperature measured at the beginning. Based on the resulting curve, further adjustments will be made.

A good estimation for the absorptivity is $A \sim 0.70$, which comes from the reflection for GaAs and air. Indeed, the cell does not have anti-reflection coating and back reflector, which means that I can use the refractive index of the semiconductor and then the relation $A=1-R$ to determine the absorptivity.

Indeed, considering the refractive index of GaAs ($n=3.8$) and air ($n=1$), the reflection can be calculated with the Fresnel equation:

$$R = \left| \frac{3.8 - 1}{3.8 + 1} \right|^2 = 34 \%$$

Consequently, the absorption can be considered around 66%.

This method might not give a good approximation, or maybe only in some wavelength range sufficiently higher than the bandgap. The EQE is a better quantity to use; however, if we don't have it, this approximation can be used to see how this parameter affects the results.

The evaluation with electroluminescence will be analyzed first. Considering all the assumptions above, with a temperature measured in the lab of 291.95 K, this is how the curve looks like (Figure 22).

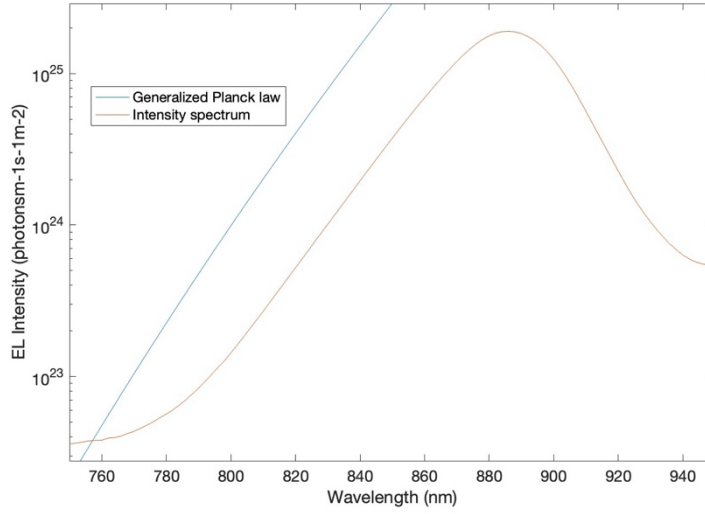


Figure 22. Generalized Planck law with $A=0.66$, $T=291.95$ and $\Delta\mu=1$ and intensity electroluminescence spectrum at $V=1V$.

As showed in the figure above, the Generalized Planck law doesn't fit the spectrum with the given parameters. This means that the value of $\Delta\mu$ that will fit the spectrum will be lower. Consequently, this value should be lower.

Lowering the voltage in the code, a fit of the curve with the spectrum is found at $V=0.95 V$. This gives a discrepancy for $\Delta\mu$ of 50 meV with respect to the value expected (which should be closer to the voltage applied, i.e. 1 V). The result is shown in Figure 23.

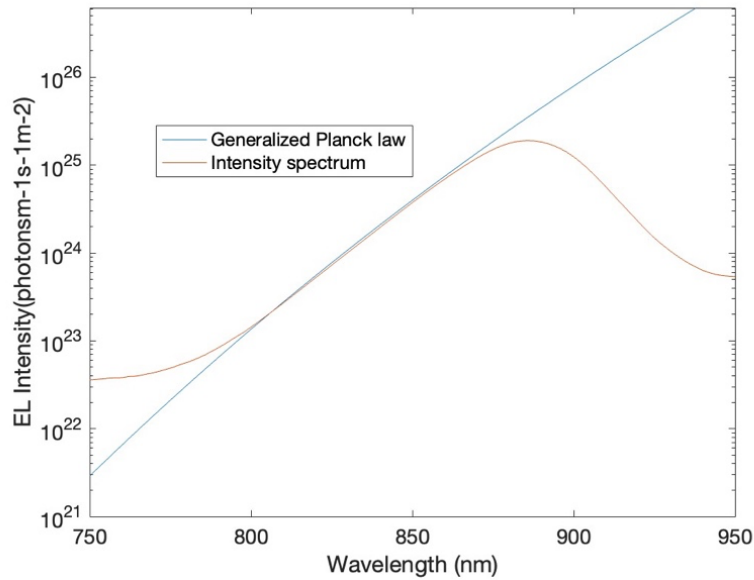


Fig 23. Generalized Planck law and electroluminescence intensity spectrum. The fit of the curve with the spectrum gives an estimation of the qfls. In this case, the fit is found for $A=0.66$ and $V=0.95$.

The same computation will be repeated for the photoluminescence spectra. Starting from the same assumptions ($A=0.66$, $T=291.95$, $V=1$), the spectrum is shown below in Figure 24.

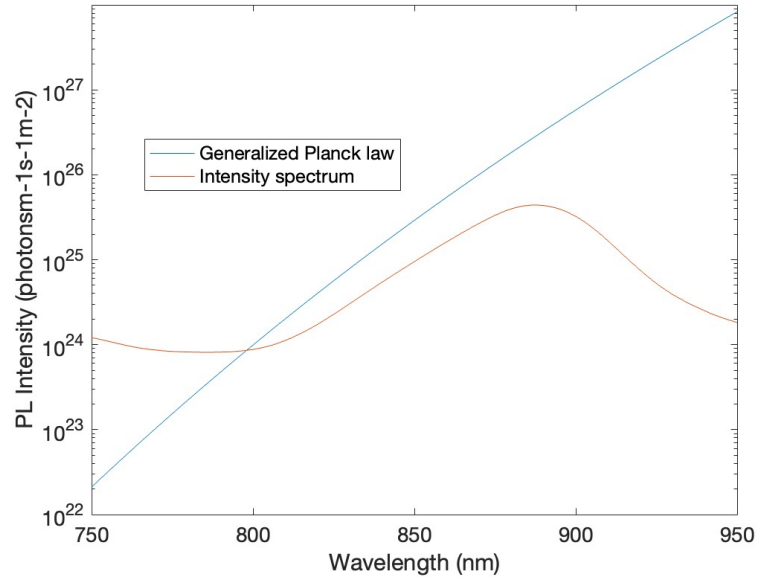


Figure 24. Generalized Planck law with $A=0.66$, $T=291.95$ and $\Delta\mu=1$ and intensity photoluminescence spectrum at $V=1$ V.

Also in this case, some adjustments are needed for the curve to fit the spectrum. Keeping $A=0.66$ and playing with the voltage, a fit is found for $V=0.97$ V (Figure 25).

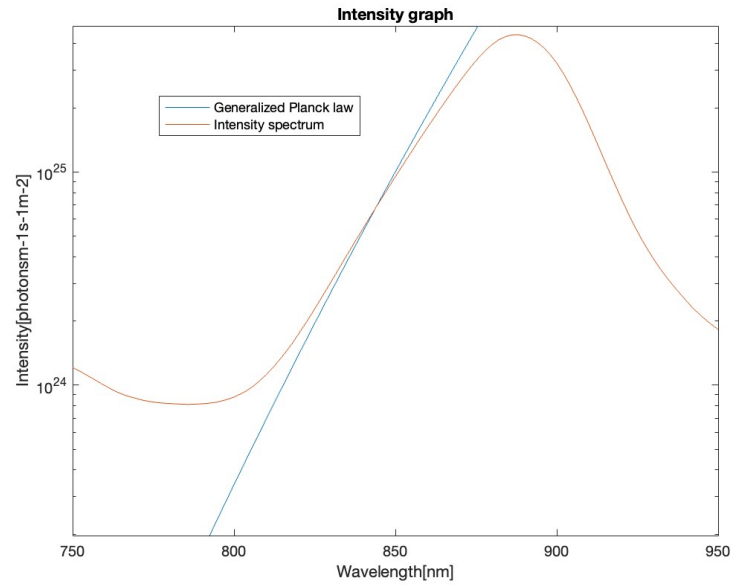


Figure 25. Generalized Planck law and photoluminescence intensity spectrum. The fit of the curve with the spectrum gives an estimation of the qfls. In this case, the fit is found for $A=0.66$ and $V=0.97$.

With photoluminescence, a discrepancy of $\Delta\mu$ is lower (30 meV, compared to 50 meV of electroluminescence).

In this case, as shown in the figure, the slope of the curve doesn't perfectly fit with the spectrum. Considering the formula of the Generalized Planck law, this can be due to the temperature. In fact, during photoluminescence measurements, an increase of

temperature within the cell may occur due to thermalization and non-radiative recombination processes.

Therefore, the temperature used to fit the spectrum can be increased. An increase in the temperature of 10 K to have a better fit leads to an increment in the uncertainty of $\Delta\mu$ of around 15 meV.

For both EL and PL measurements the estimated quasi-Fermi level splitting is lower than the one expected. In particular, for electroluminescence, with an applied voltage of 1 V, we found $\Delta\mu = 0.95$ eV, while for photoluminescence, with an open circuit voltage of 1 V, we found $\Delta\mu = 0.97$ eV.

The quasi-Fermi level splitting is considered spatially constant for these estimations. However, this might be not true. Indeed, there could be voltage drops in the depth profile from local saturation currents and local resistances. Moreover, non-realistic $\Delta\mu$ estimation could arise from the assumption of constant absorption, which might be not true. An underestimation of A leads to error in $\Delta\mu$ between 30 meV and 50 meV. To have a better estimation of the quasi-Fermi level splitting, EQE should be used instead of the absorption. In this specific case, we didn't measure it.

Discrepancies in the difference between measured temperature and fitted temperature can be also used to assess the validity of the assumptions made at the beginning.

Usually, the higher is the difference between the two temperatures, the more underestimated the qfls will be.

6.1.1.3 Images of Electroluminescence

One of the advantages of the measures of luminescence with the hyperspectral setup is that we can have not only spectral information, but also images. This allows a better understanding of the behavior of the cell, because it can help to detect local phenomena. In particular, with electroluminescence images, dark spots or areas can identify shunt and series resistances or defects such as broken busbars and fingers or degradation.

For this purpose, 3 images of electroluminescence at different voltages have been measured. In this way, it is possible to study the variation of the luminescence across the cell as a function of the voltage. Figure 26 shows the results of the experiment.

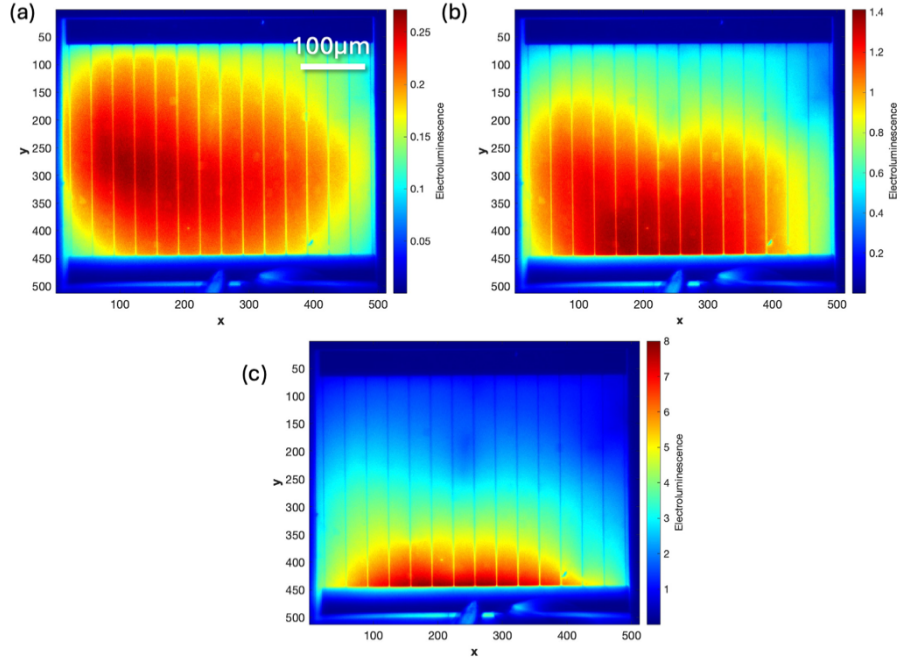


Figure 26. Maps of electroluminescence of the cell at $V=0.95$ V, $V=1$ V and $V=1.05$ V.

Starting from the up-left figure, images of electroluminescence with a variation of the voltage are shown. The first image is taken at $V=0.95$ V, and the others with an increased voltage step of 50 mV.

At the top and bottom of the cell the busbars for the contact are recognizable; in particular, at the bottom it is possible to see the tips of the probe used for the top contact. The back contact is taken on a gold plate placed below the cell. Busbars and fingers don't generate electroluminescence themselves, so the EL intensity of these regions is very low, but the areas adjacent to the fingers can show higher intensity due to efficient carrier injection.

The presence of the tips for the top contact is also recognizable by the behavior of the electroluminescence through the cell. Indeed, this is stronger increasing the voltage in the region close to the contact, because of efficient collection and distribution of current.

In this case, there are no defects or issues visible on the cell.

In addition to a comment on the map of the cell, once the different areas have been identified the variation of electroluminescence with the voltage can be discussed: as the voltage increases, the EL intensity also increases, becoming stronger close to the contact. This is because a higher voltage results in a higher current through the cell, which leads to more radiative recombination for charge carriers. Instead, away from the contacts, the luminescence drops more quickly with increasing voltage. This is because a higher lateral current leads to voltage drops due to series resistances encountered along the path, reducing the electroluminescence intensity ^[21].

6.1.1.4 Images of Transport efficiency

Once we measured electroluminescence images, transport efficiency can be computed.

As explained above, couples of electroluminescence images at slightly different bias voltages are needed. In this regard, a good voltage step between one image and

another seems to be 10 mV. Therefore, according to the measurements for electroluminescence, images at 0.95 V and 0.96 V, 1 V and 1.01 V and 1.05 V and 1.06 V are exploited. The results are shown below in Figure 27.

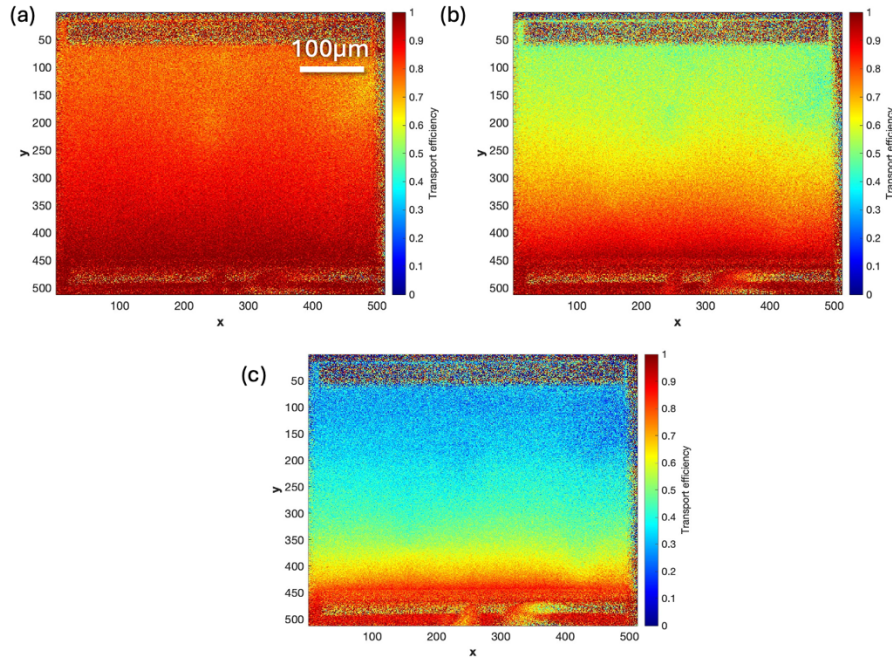


Figure 27. Maps of transport efficiency of the cell obtained with EL images at 0.95 V and 0.96 V, 1 V and 1.01 V, 1.05 V and 1.06 V.

Also in this case a variation of the transport efficiency along the cell and its behavior with the voltage can be discussed.

Figure 28 and 29 show the variation of the transport efficiency along the x and y axes respectively for the different couples of voltages.

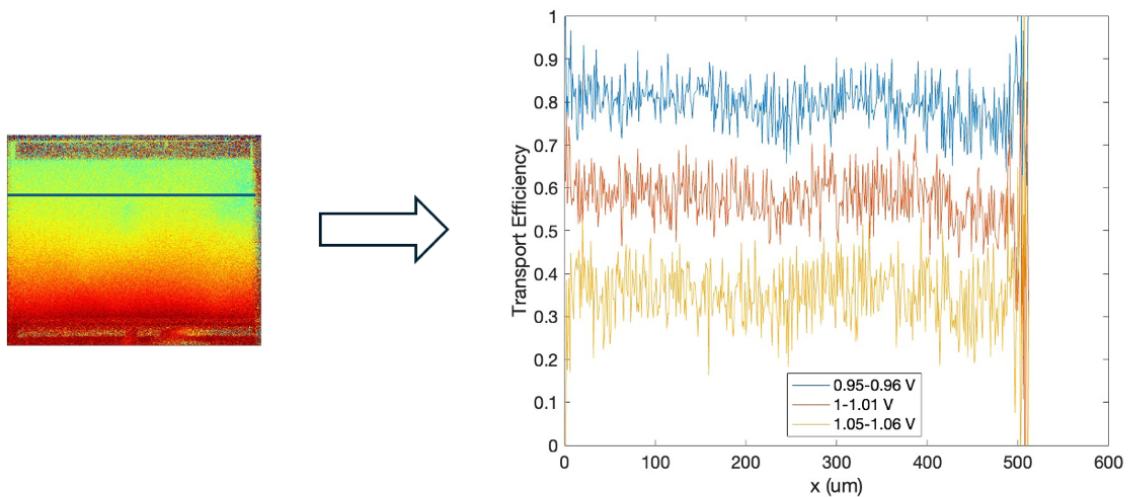


Figure 28. Profile of average transport efficiency profiles along x axis. For the x-axis, the selected row is showed in the picture on the left.

A first thing to observe is the difference between the upper and lower parts of the cell. This is consistent to what we did during the measurements. Indeed, in proximity of where the electrical contacts are placed, the efficiency seems to be higher, because

in this region the effects of resistance and recombination are minimized. Moreover, increasing the voltage the transport efficiency decreases. This is due to series resistance: at high voltage the impact of series resistance become non negligible.

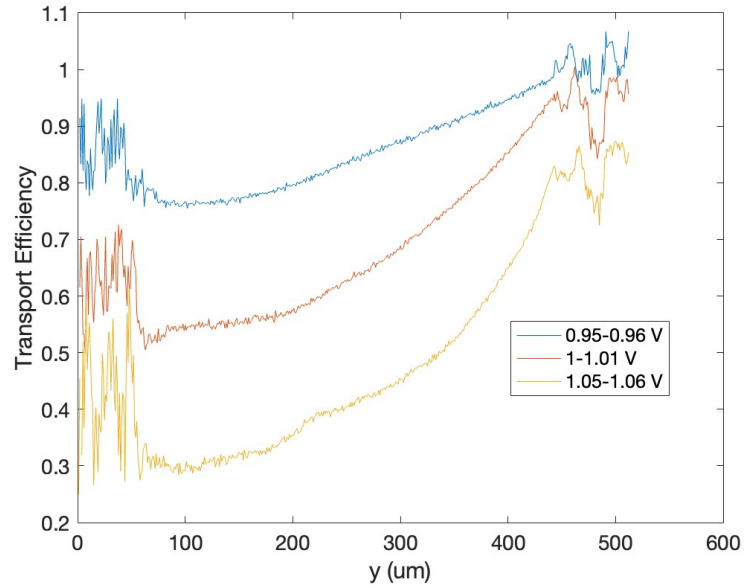


Figure 29. Profile of surface average transport efficiency along the y axis.

The voltage at which we start to have this effect can be usually checked from the dark IV curve.

The behavior of the transport efficiency as a function of the voltage is shown in Figure 30, where on the x-axis is shown the voltage applied on the cell, while on the y-axis the average transport efficiency over the surface is reported.

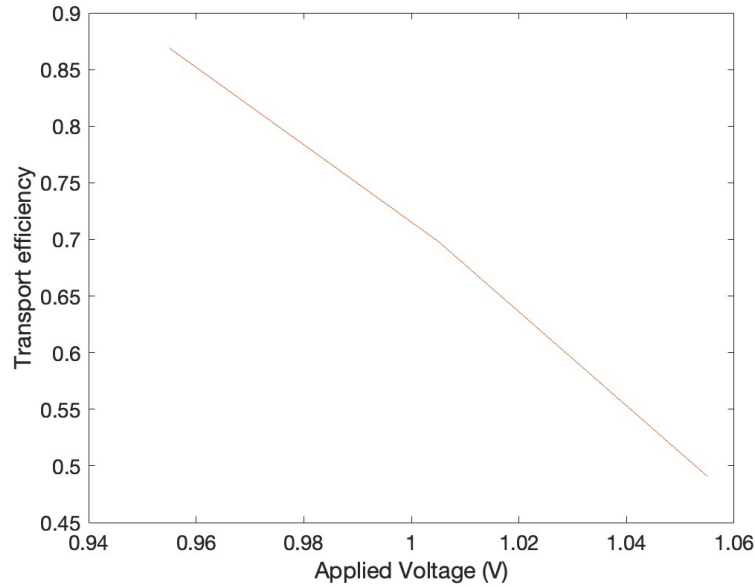


Figure 30. Surface average transport efficiency vs applied voltage over the cell.

As expected, an increased forward bias results in a reduction of the transport efficiency.

6.1.2 InGaP single junction

The same measurements are repeated for an InGaP single junction. Since there are no significant remarks on the results, these have been reported in the Appendix.

6.2 Multi-junction

In this part, measurements on tandems are exploited. The parameters studied are the same as the single junctions. What changes, in this case, is the configuration of the setup. Indeed, since we are in presence of a stack of junctions, what would be interesting is to separate the contribution of the individual layers to study them singularly. This is possible using optical filters on the collector and measuring broadband images. In fact, choosing an appropriate filter within the wavelength of interest, it is possible to isolate the subcells. Measuring cubes also works, but it takes more time.

The cell analyzed in this section is a 2-junction solar cell, with InGaP as top subcell and GaAs as bottom subcell. A schematic of the cell and a picture of the sample is shown in Figure 31.

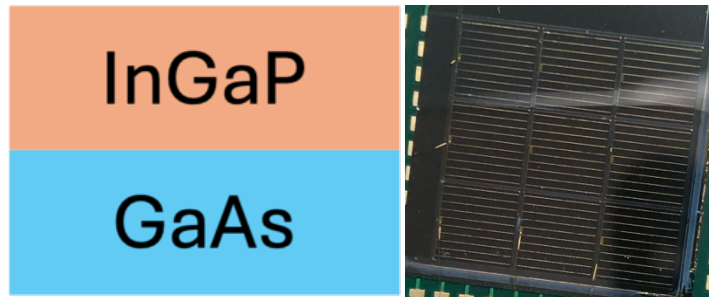


Figure 31. Schematic of the cell (left) and picture of the sample (right).

6.2.1 Setup

An appropriate choice of the optical filters can be done considering the band gap of the two materials. Indeed, knowing the band gap of the material allows to determine the wavelength at which the material absorbs or emits light, using the relation

$$E_g = \frac{hc}{\lambda} . \text{ In particular:}$$

- For InGaP: the band gap is about 1.8-1.9 eV, which means that its λ is around 650 nm
- For GaAs: the band gap is 1.42 eV, which means that its λ is around 870 nm

At this point, two choices are reasonable: using bandpass filters or a couple of long pass and short pass filters. The difference between them is that a bandpass filter allows light within a specific range of wavelengths to pass through, blocking the light outside this range, while the long pass and low pass filters allow light with wavelengths respectively longer and lower than a certain cutoff wavelength to pass through, blocking all the other wavelengths.

In this case, a reasonable choice is to use a 750 nm long pass filter to isolate GaAs and a 750 nm short pass filter to isolate InGaP. A counterproof of the validity of this choice can be obtained looking at the spectrum of the cell (it will be shown later).

6.2.2 Dark Conditions

For this first set of experiments, only electroluminescence has been measured. Photoluminescence is also possible, but as we are in presence of two junctions, different light sources are needed, and it will be discussed later.

6.2.2.1 Dark IV curve of the total cell

First, a dark IV curve of the total cell is measured to have an overview of how the total cell works varying the voltage. The behavior of the curve is shown in Figure 32.

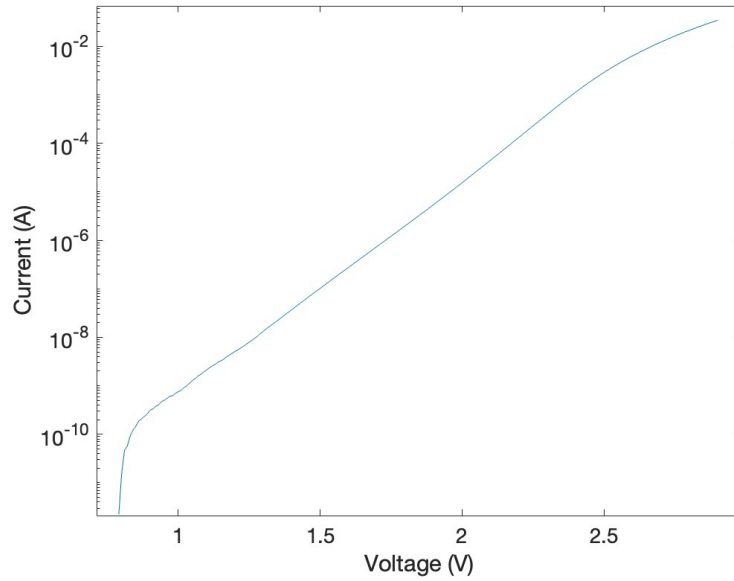


Figure 32. Dark IV curve of the total cell.

Looking at the curve of the total cell, no issues due to shunt resistance are visible at low voltages, and the effect of series resistance comes at around 2.6 V, where the curve starts to bend.

6.2.2.2 Quasi-Fermi level splitting

For the estimation of the quasi-Fermi level splitting in this case, only an electroluminescence spectrum is measured. It is possible to analyze the spectra of the cells simultaneously, so no filters are needed at this step. The voltage applied to the total cell is 2.3 V, which should be the “ideal” open circuit voltage. Indeed, the open circuit voltage of a good GaAs cell is around 1 V, while for InGaP is 1.3 V. Thus, a cube of electroluminescence at 2.3 V has been measured to plot the spectrum of the total cell. The result is shown in Figure 33.

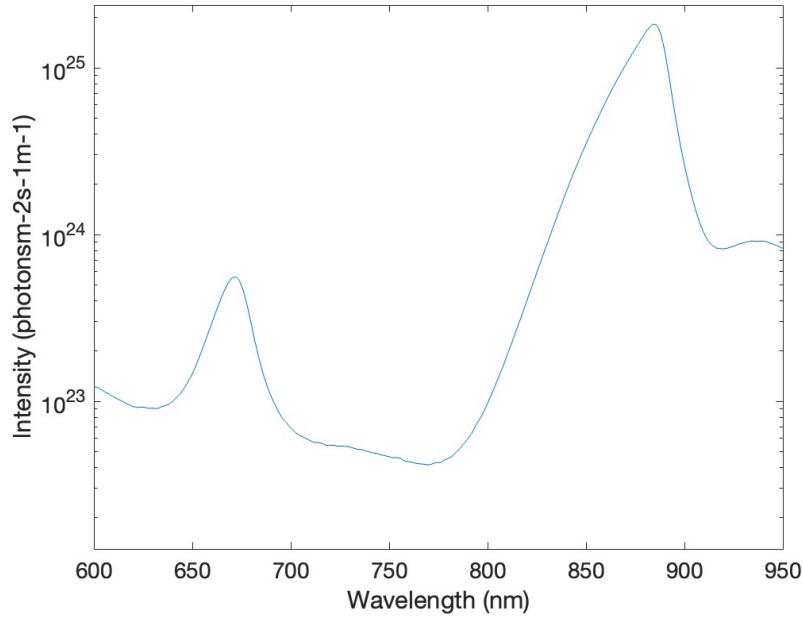


Figure 33. Electroluminescence spectrum of the total cell (average over an area of the cube). The peaks identify the top subcell as the first one on the left, while the other one is the bottom subcell.

From the spectrum two peaks are visible, which represent the emission wavelengths of the two materials. And as previously said, from the wavelength of the peak, it is possible to identify which one is the top subcell and which one is the bottom subcell. Moreover, looking at the spectrum the choice of the filters seems reasonable, since 750 nm is exactly in between the two subcells.

For the estimation of the quasi-Fermi level splitting, the same approach with the generalized Planck law used for the single junction is applied.

The cells do not have an anti-reflection coating and back reflector. The thickness of the InGaP cell is 640 nm, and that of the GaAs cell 2000 nm. With this information, we can approximate A .

This time, since we are in presence of a multi-junction with different materials, two assumptions for A will be done:

- For the top subcell, the reflection at air/InGaP interface must be computed. Knowing that $n_{\text{air}}=1$ and $n_{\text{InGaP}}=3.1$ and using the Fresnel equation, we obtain $R \approx 26\%$, which gives an absorbance $A \approx 74\%$
- For the bottom subcell, the reflection at InGaP/GaAs interface must be considered. Knowing that $n_{\text{GaAs}}=3.8$ and using the Fresnel equation, we obtain $R \approx 1\%$, which is almost negligible. Therefore, only the interface between air and InGaP is important.

According to this, supposing that the temperature of the cell increases during the experiment up to around $T=300$ K, a fit of the curve is found for $V^{\text{top}}=1.3$ V and $V^{\text{bottom}}=0.94$ V, for a total voltage of $V=1.3+0.94=2.24$ V. Figure 34 shows the fit of the spectrum for top and bottom subcells.

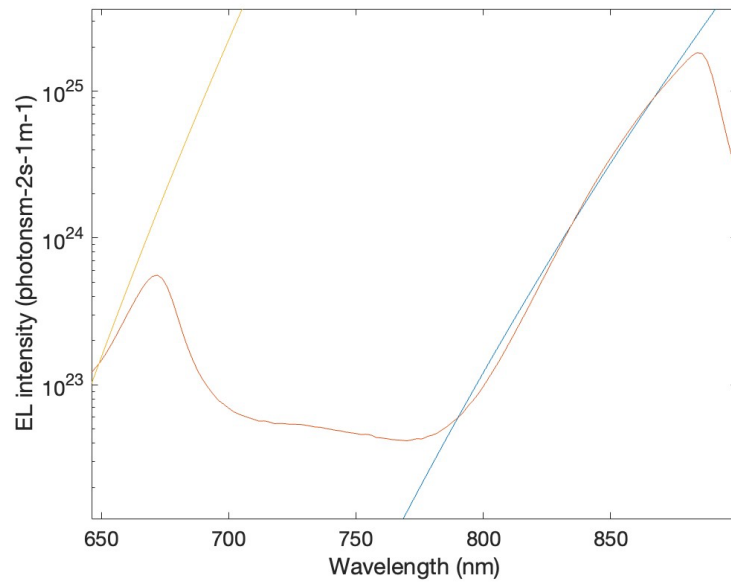


Figure 34. Fit of the Generalized Planck law for top and bottom subcell with the electroluminescence spectrum measured at $V=2.3$ V. The fit for the top subcell is found with $A^{\text{top}} = 0.74$ and $V^{\text{top}} = 1.3$ V, while the fit for the bottom is found with $A^{\text{bottom}} = 0.9$ and $V^{\text{bottom}} = 0.94$ V.

From the figure above it is possible to notice that, while for the bottom subcell the slope for the fit is quite accurate, this is not the case for the top subcell. This could be due to a different temperature distribution through the cells.

Holding the reciprocity relation, absorptivity can be substituted with EQE. In this specific case, EQE measurements are available, and they will be used to compare results.

Figure 35 shows the EQE of the subcells, which has been measured by the institute that provided the cells.

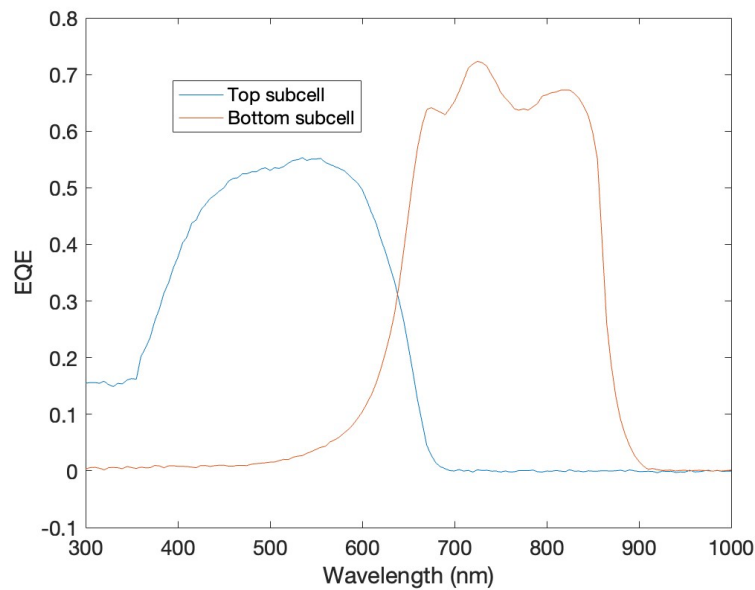


Figure 35. EQE measurements of top and bottom subcell. These measurements have been given by the institute that fabricated the cell.

The top and bottom subcells have complementary nature: the top subcell absorbs photons at shorter wavelengths, while the bottom subcell covers longer wavelengths, ensuring a broader absorption of the spectrum.

The top subcell reaches its maximum of about 0.6 around 500 nm: this is where the maximum fractions of photons are converted as electrons. Then it decreases until becoming zero at 700 nm.

The bottom subcell absorbs photons in the red and near-infrared spectrum, compensating the absorption spectrum of the top subcell. It reaches its maximum of about 0.7 around 800 nm, then it starts to decrease.

In the region between 600 nm and 700 nm, the EQE of the two cells overlap: this means that they both contribute to the absorption.

Substituting A with the EQE in the Generalized Planck law for top and bottom subcell, the best fit is found with $V^{\text{top}} = 1.32$ V and $V^{\text{bottom}} = 0.94$ V (Figure 36). This suggests that the EQE adjustment has no effect for the bottom subcell (at high wavelengths the EQE is low, so there is still a contribution of the noise), while for the top subcell is still difficult to fit the curve. This could be because the EQE of the top subcell is significantly low in this range.

The EQE measured at a particular wavelength, for example 880 nm, doesn't come from a pure light source but it is influenced also by the nearby wavelengths (a range of ± 5 nm is a possible value).

If the EQE changes rapidly, the influence from the nearby wavelengths can make the measured EQE appear less sharp than how actually is, i.e. the measured EQE might not precisely reflect the real value.

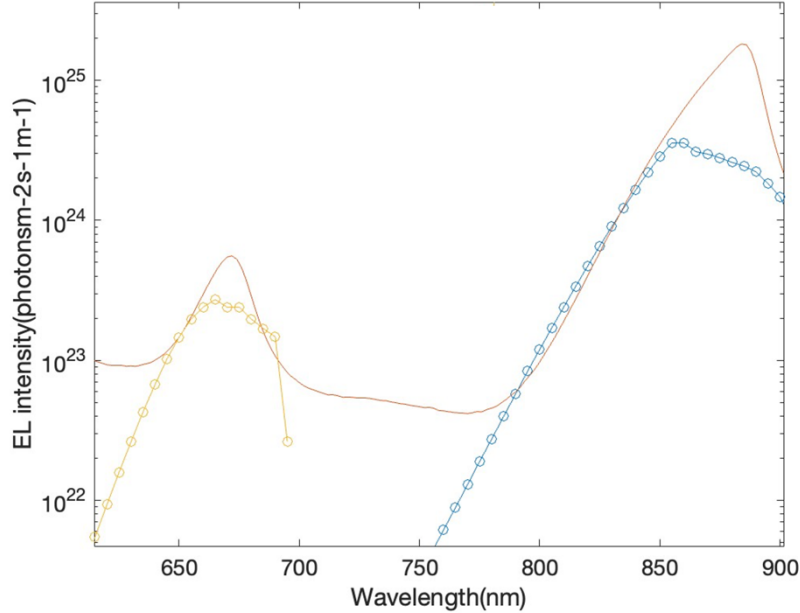


Figure 36. Fit of the Generalized Planck law for top and bottom subcell with the electroluminescence spectrum measured at $V=2.3$ V. The fit for the top subcell is found using the EQE instead of A, with $V^{\text{top}} = 1.32$ V, while the fit for the bottom is found with $V^{\text{bottom}} = 0.94$ V.

6.2.2.3 Images of electroluminescence

The electroluminescence of top and bottom subcells is measured. To analyze the subcells individually, the two optical filters discussed before are used. In this way it is possible to extract the electroluminescence images of the subcell of interest. To discuss the variation of electroluminescence with voltage, images at several points are measured: 2.2 V, 2.3 V, 2.6 V, and 2.9 V. The results for top and bottom subcells are shown respectively in Figure 37 and 38.

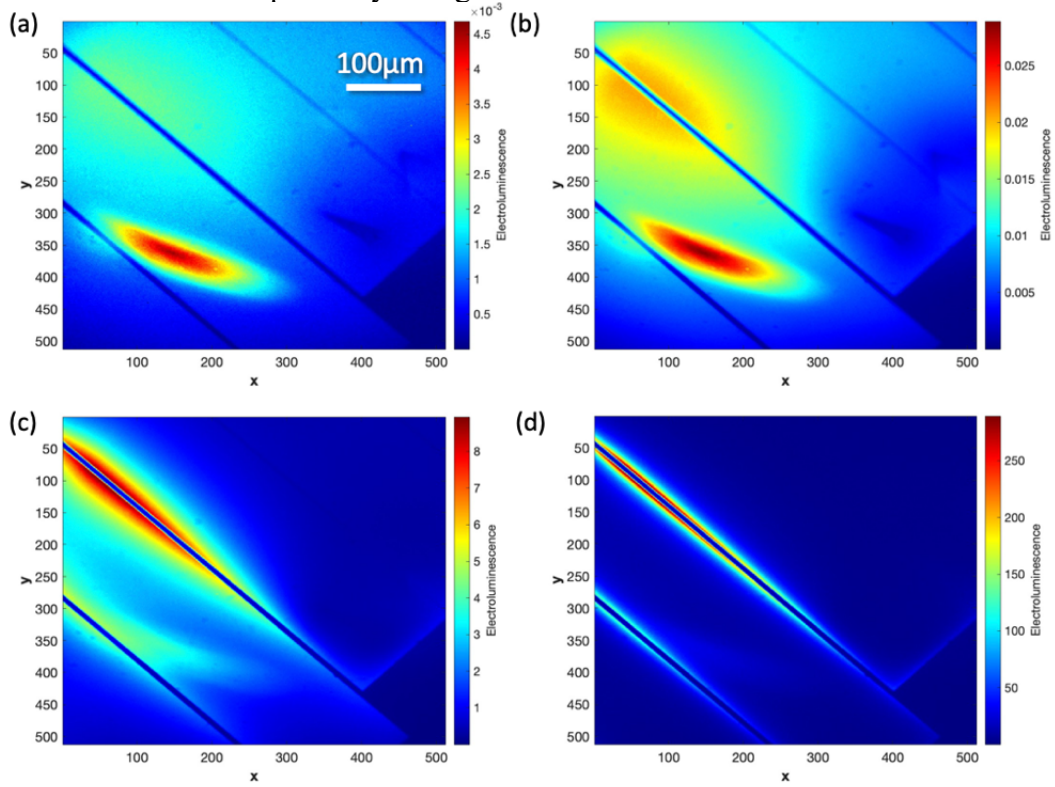


Figure 37. Electroluminescence images of the top subcell at 2.2 V (a), 2.3 V (b), 2.6 V (c) and 2.9 V (d). The subcell has been isolated using a 750 nm SP filter.

From the set of figures above, it is possible to notice that electroluminescence of the top subcell increases with the voltage. It is very low at the beginning, because the top subcell needs higher voltage to start emitting light. Then it starts to increase, and it is higher in proximity of the fingers, where it reaches its maximum, while it is very low elsewhere.

Moreover, it can be easily seen that some fingers are broken: they are visible on the map of the cell at low voltages, but increasing the voltage they become darker, since there is no carrier collection around them.

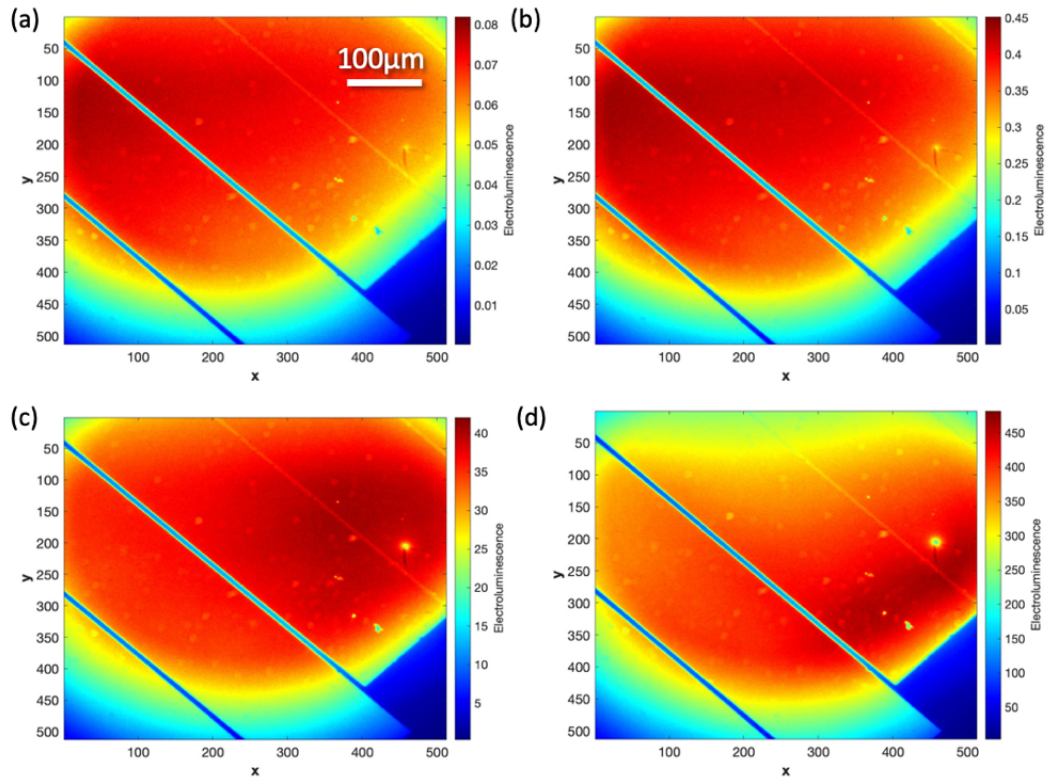


Figure 38. Electroluminescence images of the bottom subcell at 2.2 V (a), 2.3 V (b), 2.6 V (c) and 2.9 V (d). The subcell has been isolated using a 750 nm LP filter.

For the bottom subcell the electroluminescence is more uniform across the area, and it is possible to observe it at low voltages, since the bottom subcell requires a lower voltage to bias the junction and emits light. Also, the effect of the broken fingers is still visible.

6.2.2.4 Images of transport efficiency

Once electroluminescence images are measured, maps of transport efficiency and their variation with voltage can be extracted. The EL images to compute the maps have been taken at 2.2-2.21 V, 2.3-2.31 V, 2.6-2.61 V, 2.9-2.91 V. Results are shown in Figure 39 for top subcell and Figure 40 for bottom subcell.

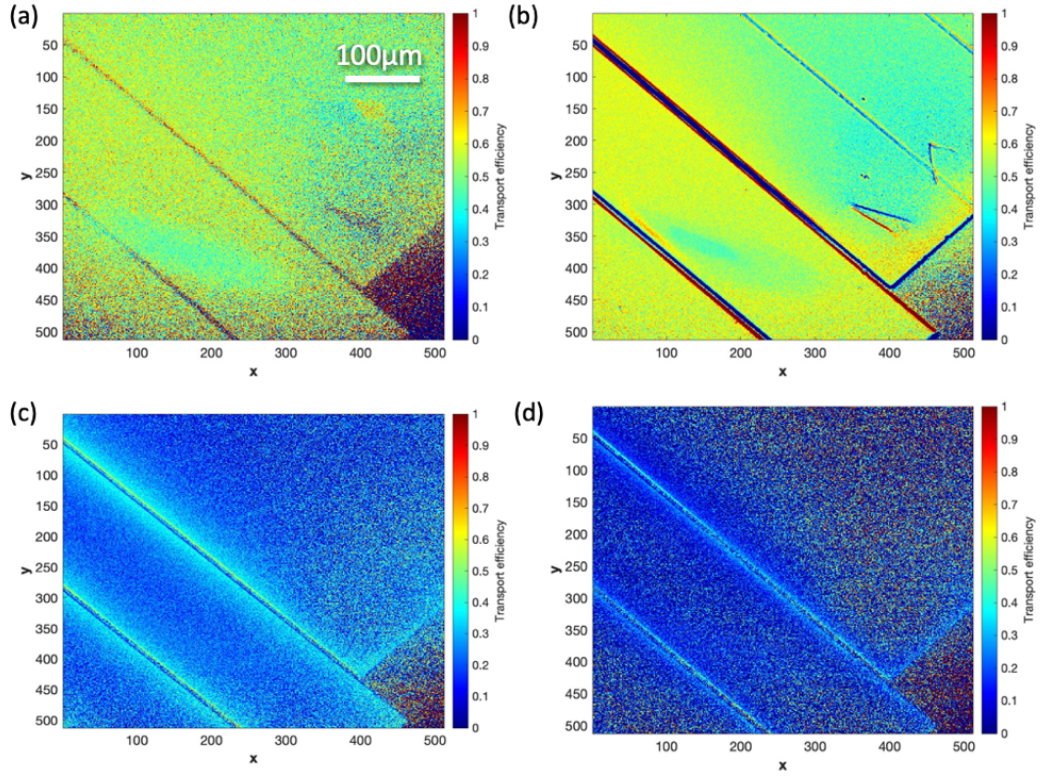


Figure 39. Images of transport efficiency of the top subcell at 2.2-2.21 V (a), 2.3-2.31 V (b), 2.6-2.61 V (c) and 2.9-2.91 V (d). The subcell has been isolated using a 750 nm SP filter.

From the images of the top cell, it is possible to notice that there is a reduction of the current collection away from the contact. This behavior is enhanced increasing the voltage, close to 2.6 V, where the cell is affected by series resistances.

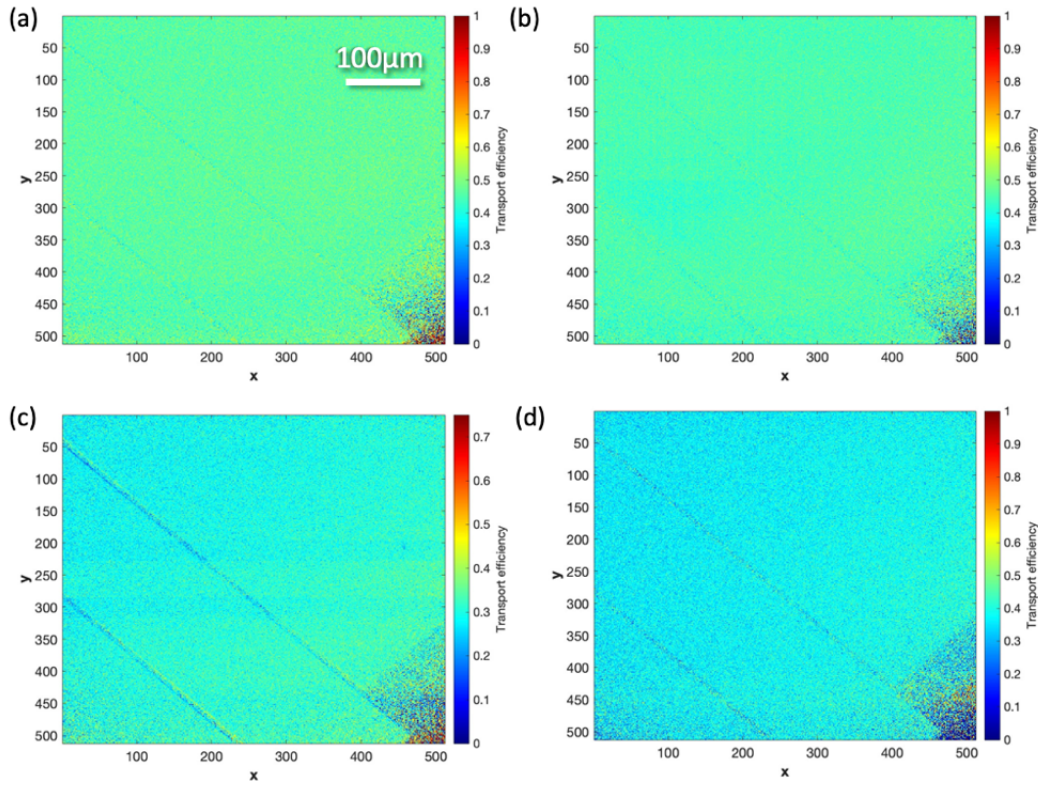


Figure 40. Images of transport efficiency of the bottom subcell at 2.2-2.21 V (a), 2.3-2.31 V (b), 2.6-2.61 V (c) and 2.9-2.91 V (d). The subcell has been isolated using a 750 nm LP filter.

From the images of the bottom cell, no issues are visible.

As explained above, the transport efficiency can be recorded not only with maps, but averaging over the area of the cell, it is possible to study the behavior of the transport efficiency as a function of the voltage. The results are shown in Figure 41 for top and bottom subcell.

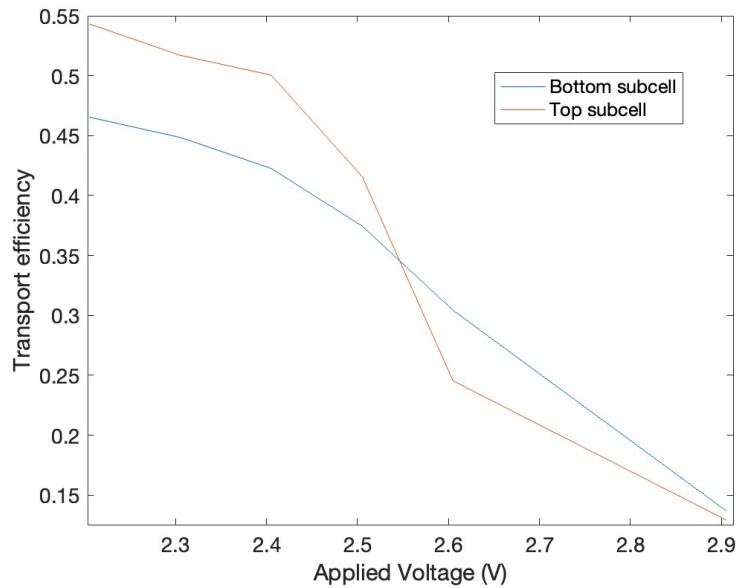


Figure 41. Surface averaged transport efficiency of top and bottom subcell vs. applied voltage.

At low voltages, carriers are efficiently collected. As the voltage increases, the increase of non-radiative recombination and series resistances limit the current flow, affecting the transport efficiency. From the dark IV curve of the cell it is predictable that the effect of series resistance should affect the cell around 2.6 V. In this case, the reduction in the collection efficiency appears around 2.4 V. This means that other carrier loss mechanisms could affect the cell.

6.2.2.5 Single subcells IV curves

To better understand the behavior of each subcell, it would be useful to extract the dark IV curves of the singles. That would also allow to use the diode equation to extract intrinsic parameters of the cell, such as the saturation current density and the ideality factor.

As explained above, a tandem solar cell is a stack of single junctions, where the total current is the same through all the cells, while the total voltage is the sum of the voltages of singles.

Deriving the single subcells IV curve is possible, taking advantage of electroluminescence images and quasi-Fermi level splitting ^[19,20].

Indeed, the luminescence emission at a given position (x, y) can be written as

$$\phi_{em}(x, y) = C(x, y) \exp\left(\frac{qV(x, y)}{kT}\right) \quad (13)$$

where C(x, y) is a position-dependent calibration constant (we are measuring broadband images, so the black-body flux cannot be estimated) and it is assumed to be the same through the subcell of interest, and V(x, y) is the internal voltage computed at the position (x, y). Rearranging for the voltage, this leads to

$$V(x, y) = \frac{kT}{q} \ln\left(\frac{\phi_{em}(x, y)}{C(x, y)}\right) \quad (14)$$

Measuring an image of electroluminescence, this relation can be solved for the internal voltage, giving the relation

$$V(x, y)^{applied} = V(x, y)^{computed} - C(x, y) \quad (15)$$

where

- $V^{applied}$ is the voltage applied to measure the image
- $V^{computed}$ is the relative internal voltage derived from the electroluminescence image

Measuring a set of electroluminescence images at different voltages, it is possible to plot a graph where on the x-axis there is the voltage applied to measure the electroluminescence image, and on the y-axis there is the internal voltage extracted from the formula.

If C is constant through the subcells, it is sufficient to determine it for one couple of $V^{applied}$ and $V^{computed}$ at a given position for the top and the bottom subcell, and then substitute it into the equation for all the voltages to reconstruct the subcells IV curve. The current for each subcell is the same as the total cell, because in a tandem the total voltage is given by the sum of the single voltages of the subcells, while the total current is shared between them.

The point chosen to determine C is the same at which we estimate qfls, because it gives precisely the real voltage applied to the cell. Figure 42 shows an example of how the graph looks like. Increasing the applied voltage, the relative internal voltage that will be computed increases, while C is kept constant. The resulting curve is a steep slope.

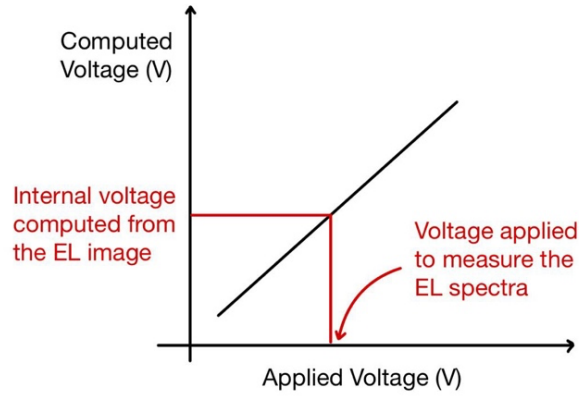


Figure 42. Schematic representation of how the curve of the internal voltage computed as a function the applied voltage looks like. The curve is a steep slope, because increasing the applied voltage, the voltage computed is also expected to increase, while C remains constant. Knowing the value of the qfls estimated (V^{applied}) at a certain voltage applied to take the EL spectrum, it is possible to use it in combination with the internal voltage found at the same value (V^{computed}) to compute the calibration constant C with the formula $V^{\text{applied}}(x,y) = V^{\text{computed}}(x,y) - C(x,y)$.

The steep slope represents the internal voltage computed at each voltage applied to measure an electroluminescence image. If we look at the value of the voltage applied to measure the electroluminescence spectrum, it is possible identify its corresponding internal voltage. But this value is a relative voltage, as it must be shifted by a constant C . And we know that at this applied voltage, the expected one to be found has been determined with the qfls estimation.

The plot of V^{computed} vs V^{applied} and the estimation of C for both top and bottom subcell are reported below.

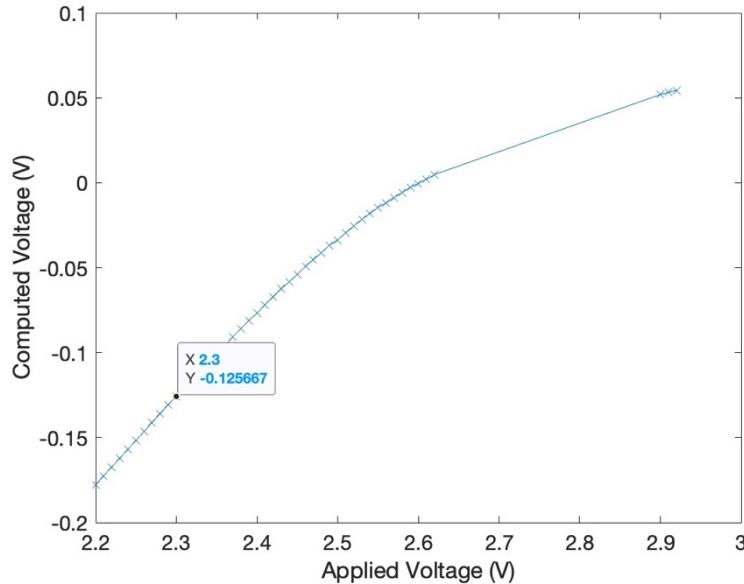


Figure 43. Internal voltage extracted at each image of electroluminescence measured for the top subcell. The crosses indicate the points measured.

Figure 43 shows on the x-axis the voltage applied to measure the electroluminescence image and, on the y-axis, the corresponding internal voltage calculated with (14).

For the image of electroluminescence measured at 2.3 V, the relative internal voltage computed is -0.125 V. But from the estimation of the qfls, we know that at 2.3 V, the contribution of the voltage from the top subcell is 1.28 V. Substituting into (15)

$$1.28 = -0.125 - C \rightarrow C = -1.41$$

The same steps are repeated for the bottom subcell.

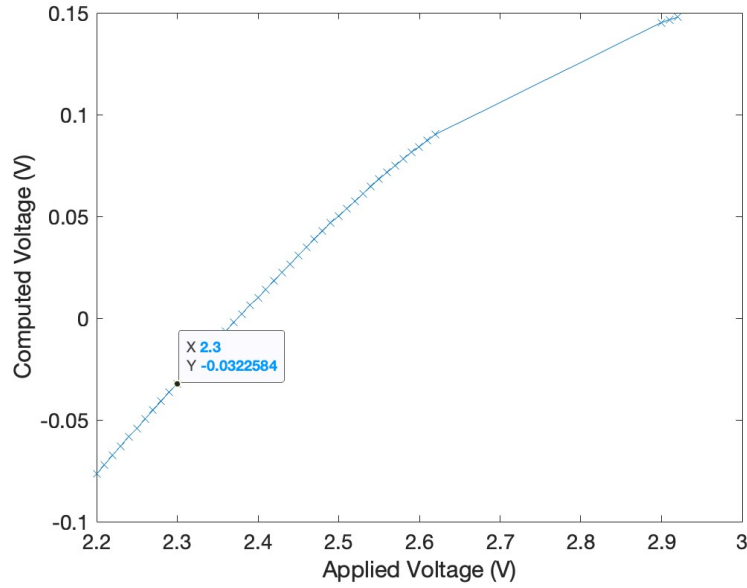


Figure 44. Internal voltage extracted at each image of electroluminescence measured for the bottom subcell. The crosses indicate the points measured.

For the bottom subcell, at the electroluminescence image measured at 2.3 V corresponds a relative internal voltage of -0.032 V. But from the estimation of the qfls, we know that the contribution of the bottom subcell is 0.95 V. Therefore

$$0.95 = -0.032 - C \rightarrow C = -0.98$$

Once the values of C for top and bottom subcell are found, the single subcells dark IV curve is extracted. The result is shown in Figure 45.

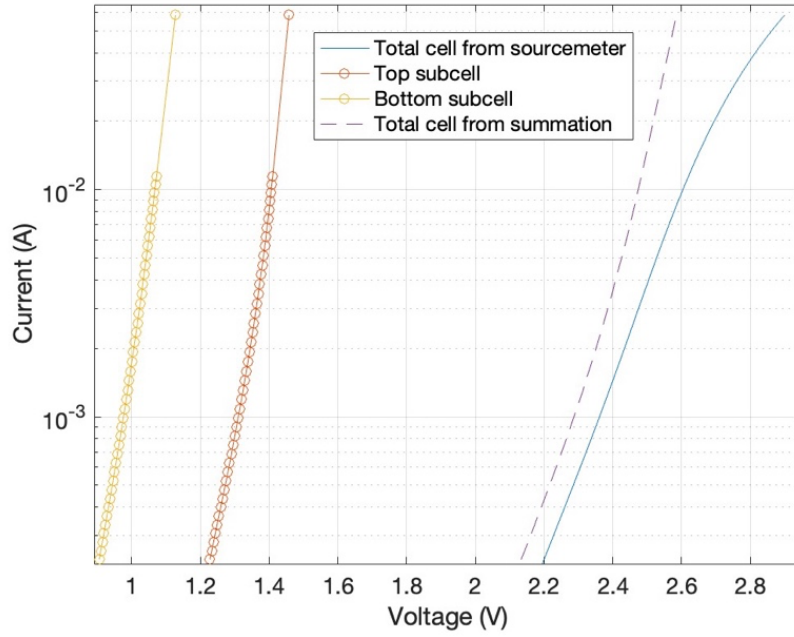


Figure 45. Single subcell dark IV curves extracted from electroluminescence measurements. The curve with dashed lines is the total cell dark IV curve obtained from the summation of the single cells, while the blue curve is the dark IV curve of the total cell measured from a continuous measure with a sourcemeter.

As it is shown in the figure above, the current is the same through the cells, while the voltages vary for top and bottom subcell. A summation of the two curves gives the total cell IV curve. This curve should overlap with the initial dark IV found for the total cell. In this case, as it is possible to notice, the two curves don't overlap, which is reasonable, because of the inconsistency found in the estimation of $q\phi_s$.

Once we have the single subcells IV curve, a fit with the simplified 2-diode equation model can be used to extract the saturation current density j_0 and the ideality factor n of each cell.

$$J(V) = j_{01} \left[\exp\left(\frac{qV}{n_1 kT}\right) - 1 \right] + j_{02} \left[\exp\left(\frac{qV}{n_2 kT}\right) - 1 \right] \quad (16)$$

The fitting of the curves is shown in Figure 46 and, knowing that the area of the cell is 0.25 cm^2 , it gives:

- For the top subcell: $J_{01}^{\text{top}} = 3.85 \times 10^{-26} \text{ A/cm}^2$, $n_1^{\text{top}} = 1$, $J_{02}^{\text{top}} = 1.78 \times 10^{-11} \text{ A/cm}^2$, $n_2^{\text{top}} = 2.7$
- For the bottom subcell: $J_{01}^{\text{bottom}} = 1.25 \times 10^{-20} \text{ A/cm}^2$, $n_1^{\text{bottom}} = 1$, $J_{02}^{\text{bottom}} = 2.06 \times 10^{-11} \text{ A/cm}^2$, $n_2^{\text{bottom}} = 1.9$

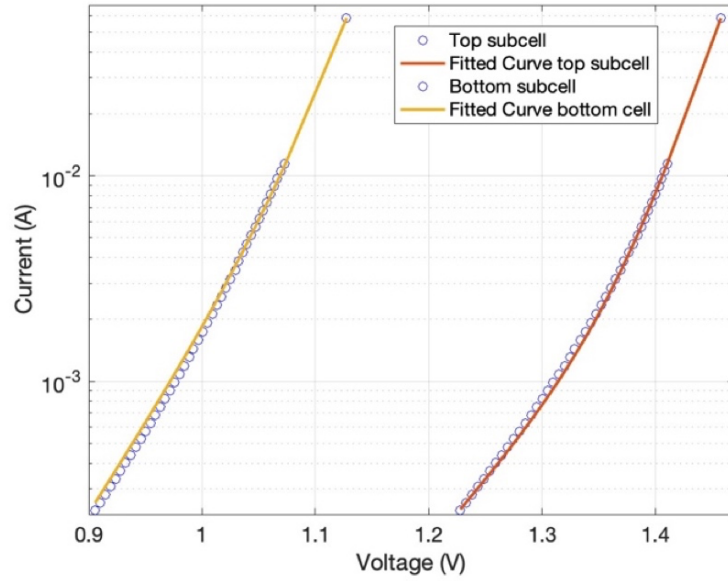


Figure 46. Fitting of the diode equation for the subcells to extract saturation current density and ideality factor. The fit for the top subcell is found for $J_{01}^{\text{top}} = 9.65\text{e-}27$ A, $n_1^{\text{top}} = 1$, $J_{02}^{\text{top}} = 4.46\text{e-}12$ A, $n_2^{\text{top}} = 2.7$. The fit for the bottom subcell is found for $J_{01}^{\text{bottom}} = 3.13\text{e-}21$ A, $n_1^{\text{bottom}} = 1$, $J_{02}^{\text{bottom}} = 5.14\text{e-}12$ A, $n_2^{\text{bottom}} = 1.9$.

The orders of magnitude of the parameters extracted are compared with the ones found in literature ^[15] and they are shown in table 3.

Parameter	Value extracted from the fitting (fig 45)	Values found in literature ^[15] , extracted with the same method
J_{01}^{top} [A/cm ²]	3.85e-26	2.07e-26
J_{02}^{top} [A/cm ²]	1.78e-11	6.49e-16
n_1^{top}	1	1
n_2^{top}	2.7	1.82
J_{01}^{bottom} [A/cm ²]	1.25e-20	3.96e-20
J_{02}^{bottom} [A/cm ²]	2.06e-11	2.24e-11
n_1^{bottom}	1	1
n_2^{bottom}	1.9	1.88

Table 3. Comparison between the values extracted from the fitting in Figure 45 and the values found in literature for the same subcells which have been extracted using the same method.

As it is shown in table 3, almost all the values have the same order of magnitude. Some differences, for example for the value of J_{02}^{top} and n_2^{top} might be due to increased recombination effect in that region for the InGaP cell that are less pronounced in the cell analyzed in the literature, different measurement conditions or different material quality. Moreover, the subcell IV curves extracted can be subject to discrepancies coming from an incorrect estimation of the qfls.

6.2.3 Under illumination

The behavior of the cell under illumination is also exploited. Since we are in presence of a tandem solar cell, a proper light source must be chosen. Indeed, the cell absorbs photons with an energy $E > E_g$.

For this part of experiments only the top cell is placed under illumination. The light source used for illuminating the cell is a blue LED 425 nm.

The filters used to analyze the single subcells have been slightly changed:

- For the top subcell, the same 750 nm SP filter as before is used
- For the bottom subcell, a 800 nm LP filter is chosen

The spectra showed in this section are not calibrated, since they're not the focus of these experiments and they have been measured just for a better understanding of the results.

In particular, the parameter that we aim to analyze under illumination is the transport efficiency. The effect of the transport efficiency of a tandem under illumination have not been studied widely in literature.

There is some literature about the application of this technique with tandems ^[15].

This will be our starting point to compare and justify the results.

Figure 47 shows the studies of transport efficiency of an InGaP/GaAs/InGaAs 3J solar cell by Xu et al. The cell is placed under 1 sun illumination so that the middle subcell is the limiting one, i.e. it has the lowest photogeneration current.

When the applied voltage is low, the non-limiting subcells operate close to their open circuit voltage. This means that f_T is low, because the local voltage variation is small with respect to the variation in V_T , which means that there is no current collection.

For what concerns the limiting subcell, its transport efficiency is high and close to 1.

As the voltage increases, the local diode voltage of the non-limiting subcells increases, becoming more effective in the current collection. Simultaneously, the limiting subcell doesn't restrict the carrier transport anymore, and the f_T decreases.

However, this behavior stops at high voltages, as the subcells start to be influenced by series resistance effects.

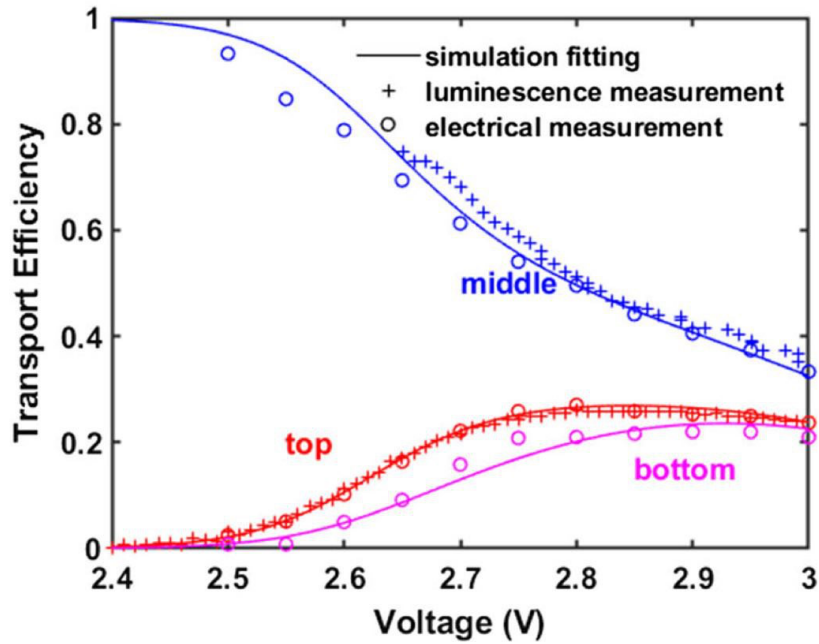


Figure 47. Spatially averaged transport efficiency of a 3J cell under 1 sun illumination as a function of the applied voltage reproduced from [15]. Electrical measurements and simulation fitting are used to be compared with luminescence results.

The same reasoning is applied to the study of the 2J solar cell of interest.

To sum up, the steps performed for measuring the transport efficiency under illumination are as follows:

1. IV curve of the total cell under illumination
2. Measurement of the cell's spectrum extracted from a photoluminescence data cube
3. Measurement of electroluminescence images under illumination and computation of transport efficiency.

As will be highlighted by the following results, the outcomes differ from expectations, leading to certain hypotheses to solve the issue. Specifically, the focus will be on the bottom subcell, but the understanding that these hypotheses can also be considered valid for the top subcell.

The issues rely on the background noise, which cannot be completely removed, and this problem is still discussed within the scientific community when luminescence is measured. There are some methods to reduce the background, but sometimes they are not enough. Based on the results achieved, some strategies will be proved to overcome the noise. Basically, they will consist of working on the spectral information, trying to reconstruct mathematically the spatial one. And depending on what we find, a solution will be discussed step-by-step.

The intensity of the LED used during all the experiments is showed in Figure 48. Along with this one, the IV curve of the cell under this illumination source has been taken and it is also showed.

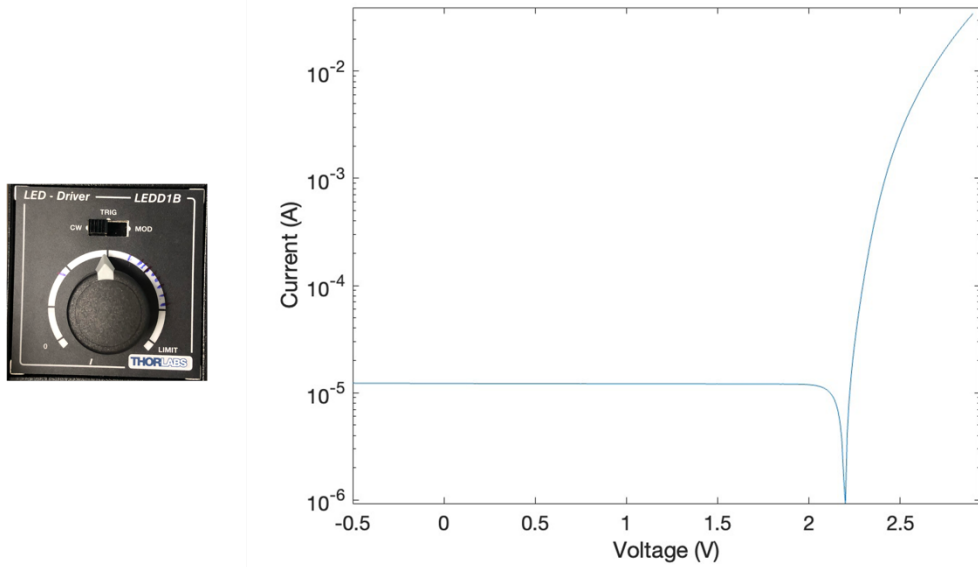


Figure 48. Intensity of the LED to illuminate the cell (left), and IV curve of the cell in dark and under illumination of the LED (right).

The method discussed above to compute transport efficiency can be also applied when the cell is under illumination. The validity of the experiments has been already proved with single junctions at different illuminations and applied voltages, showing a good agreement with electrical method and simulations.

In this experiment, we are illuminating the top subcell, which means that the bottom subcell will be the limiting one.

Therefore, we should expect this response: at low voltages, the bottom subcell is high and close to 1, while the top subcell is close to 0. Increasing the voltage, the bottom subcell decreases, while the top subcell increases with a symmetric behavior.

The points analyzed to measure the transport efficiency under illumination are the same of the ones exploited in dark conditions: 2.2-2.21 V, 2.3-2.31 V, 2.6-2.61 V, 2.9-2.91 V.

First, the spectrum of the cell under illumination is measured. To do so, the cell is placed in open circuit conditions, and an acquisition of a cube is performed. The result is shown in Figure 49.

As only the top subcell is under illumination, the peak of InGaP is the only one noticeable in the spectrum.

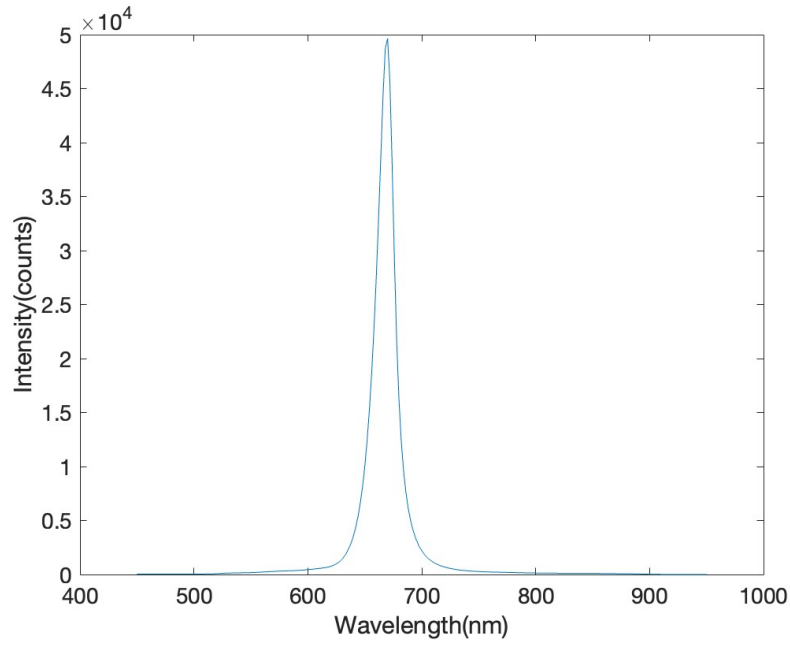


Figure 49. Spectrum of the cell under illumination over a range from 450 to 950 nm, with a 2 nm step. Open circuit voltage conditions ($I=0$ A, $V=2.18$ V)

Afterwards, images of electroluminescence are measured, and transport efficiency is computed with (10). Results of maps of f_T and surface averaged f_T versus voltage are shown below for top and bottom subcell (Figure 50, 51, 52)

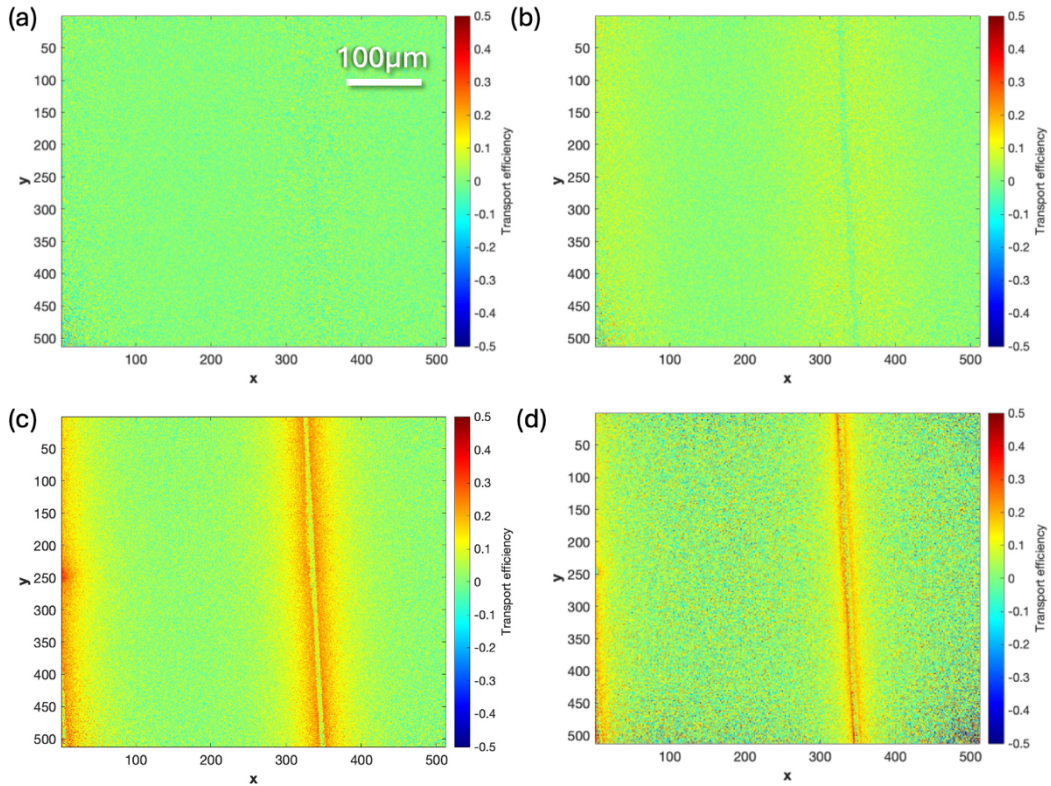


Figure 50. Images of transport efficiency of the top subcell at 2.2-2.21 V(a), 2.3-2.31 V (b), 2.6-2.61 V (c) and 2.9-2.91 V (d). The subcell has been isolated using a 750 nm SP filter.

The value of the transport efficiency of the top subcell should be 0 at low voltages, while it should increase with the voltage. Looking at the map, despite at low voltage we found that the transport efficiency is about 0, increasing the voltage f_T is still very low, and the maps there are some points on the map which have negative values.

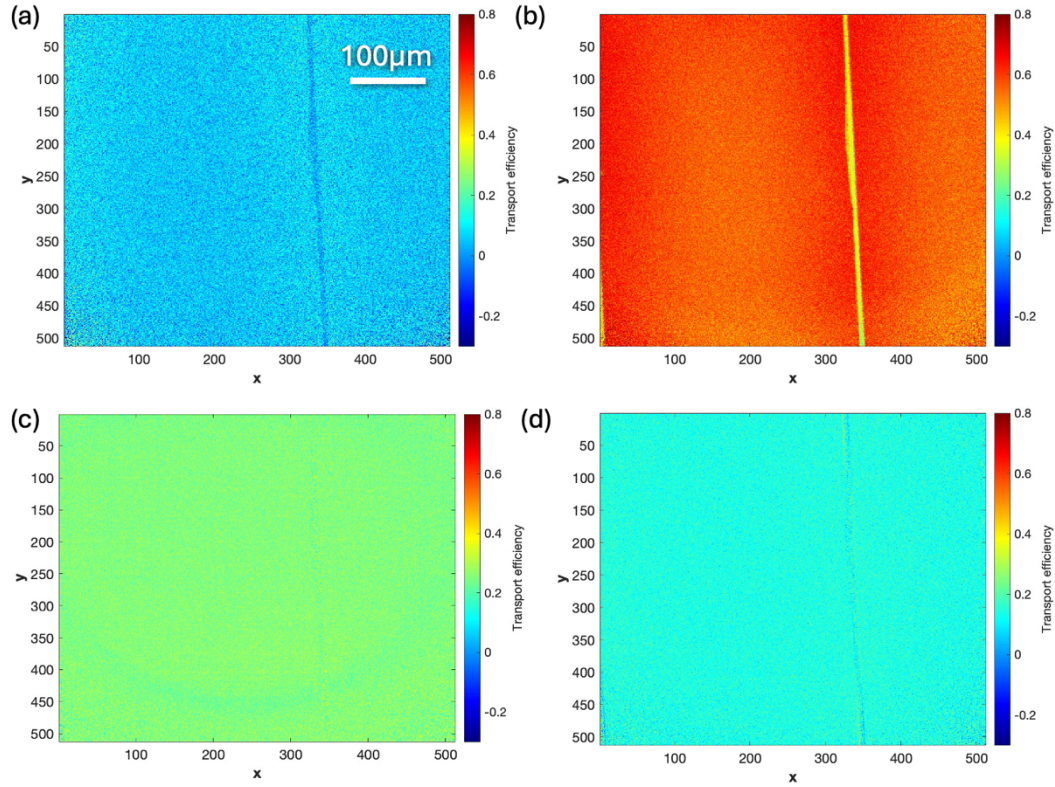


Figure 51. Images of transport efficiency of the bottom subcell at 2.2-2.21 V (a), 2.3-2.31 V (b), 2.6-2.61 V (c) and 2.9-2.91 V (d). The subcell has been isolated using a 800 nm LP filter.

The value of the transport efficiency of the bottom subcell should be 1 at low voltages, while it should decrease increasing the voltage. Nevertheless, at low voltage the f_T is very low, then there is a peak around 2.3 V, and then it decreases again.

The average of the transport efficiency over the surface seems to solve the problem of the negative values, indeed all the values coming from the average are positive, but the values are still too low. In particular, for the bottom subcell, the behavior of the curve of the average transport efficiency as a function of the applied voltage must be analyzed.

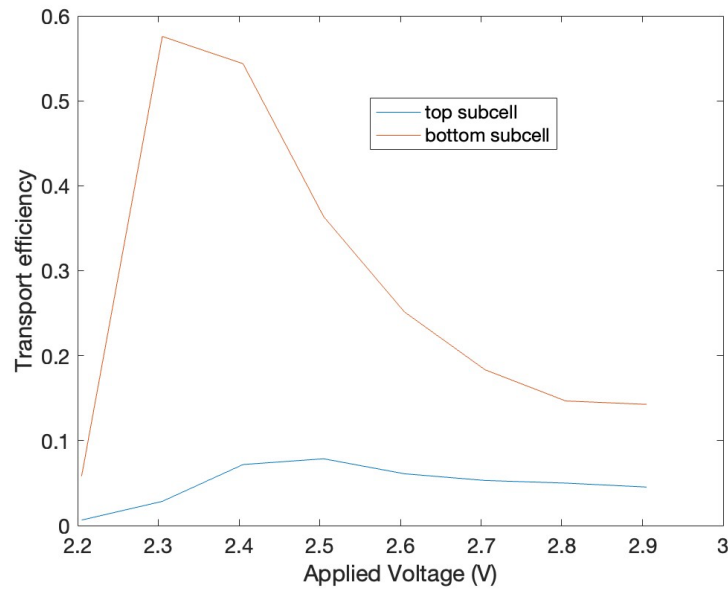


Figure 52. Surface average of transport efficiency of bottom subcell versus voltage.

As explained above, for what concerns the bottom subcell, which is in this case the limiting cell, at low voltages the transport efficiency should be high and close to 1. However, Figure 52 shows that this is not the case: at 2.2 V, the transport efficiency appears to be very low compared to what we expect.

To understand better what happens, the spectrum of the bottom subcell is taken under open circuit conditions, which is around 2.17 V. The result is shown in Figure 53.

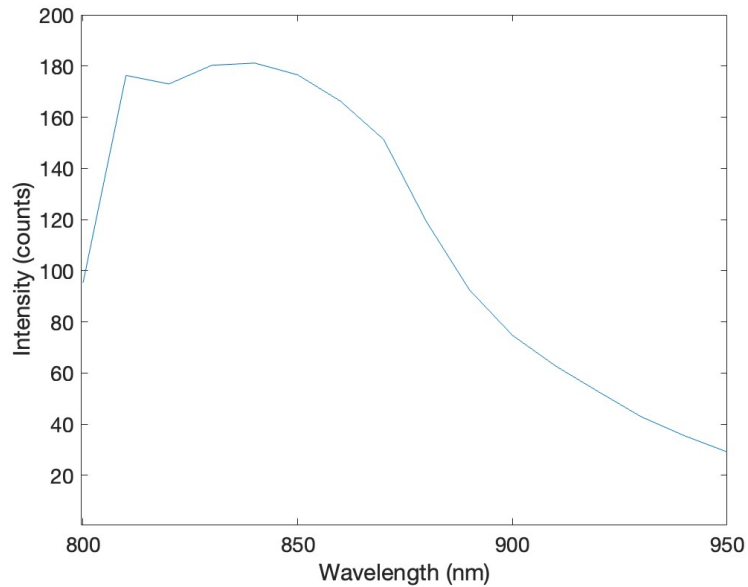


Figure 53. Intensity graph of the bottom subcell under illumination in open circuit conditions.

As it is possible to notice, the curve showed in Figure 53 doesn't seem like a signal of luminescence from GaAs. Indeed, this is background noise coming not from the cell.

The spectrum plotted above is the result from a cube of luminescence after a dark subtraction of an image at a wavelength close to where we expect to see luminescence (in this case, an image at 820 nm has been taken).

The effect of the background on the transport efficiency can be explained mathematically. The transport efficiency computed as a function of two luminescence images at voltage V_1 and V_2 is

$$f_T(x, y) = \ln \left(\frac{\phi_{EL}(V_2)}{\phi_{EL}(V_1)} \right) \quad (17)$$

Considering the influence of the background B , which we assume to be constant, f_T becomes

$$f_T(x, y) = \ln \left(\frac{\phi_{EL}(V_2) + B}{\phi_{EL}(V_1) + B} \right) \quad (18)$$

If B is high, the luminescence is considered negligible with respect to it, and so this results in zero (or close to zero) transport efficiency.

Issues related to background noise have been already exploited in the past and they are still an open question for the experts working with luminescence, because it's hard to get rid of them. There are some tricks that can be applied to reduce this effect of the background, but besides them, it's not possible to avoid it completely. Some methods to solve the reduce the noise are:

- Use a SP filter on the LED
- Compute transport efficiency using cubes instead of images
- Use a laser as light source. However, this method should be avoided when possible because the choice of a LED is cheaper and safer (indeed using a LED there are less risks not only for who works but also for the cell, because with a laser light there are more possibilities to damage it)

The first trick is to use a short pass filter on the LED. The LED that we are using is a 405 nm blue LED, which means that it emits light over a broad spectrum with a peak of intensity at 405 nm. It can happen that longer wavelengths can introduce noise. To avoid that, a short pass filter is put in front of the LED source so that only the desired wavelengths pass. This minimizes the overall noise in the system.

For this purpose, a 500 nm SP filter has been placed in front of the LED. Figure 54 shows the reduction of intensity with the filter.

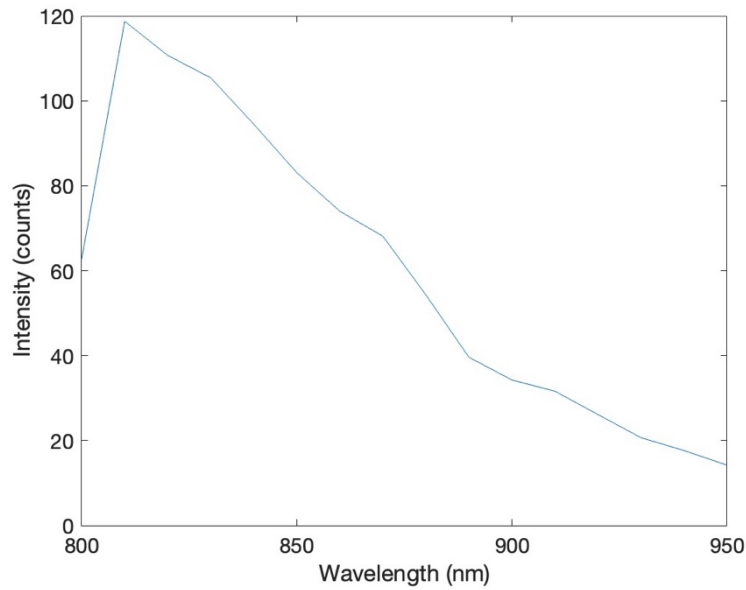


Figure 54. Intensity graph of the bottom subcell under illumination in open circuit conditions with a 500 nm SP filter on the LED.

As we see from Figure 54, there is a reduction of the signal with respect to Figure 53, where it is shown the intensity graph of the bottom subcell in the same conditions but without the filter on the LED. However, this is not enough to improve the transport efficiency at 2.2 V.

Another way to try to reduce the influence of the background is to compute transport efficiency measuring cubes of electroluminescence instead of using images.

The advantage of measuring cubes instead of images is the spectral information.

Indeed, images are measured in a broadband configuration, and the results obtained is in a 2D (x, y) form. Measuring cubes, the wavelength range of interest can be tuned to be around the wavelengths of interest. In this way, the result obtained is in a 3D (x, y, λ) form. This means that for each pixel (x, y), the spectral information at the wavelength range of interest is also captured. After, with a manual integration over the wavelengths, transport efficiency can be obtained, giving a more accurate result.

Unfortunately, also applying this method, the signal at 2.2 V is still too noisy to compute transport efficiency.

One trick to reduce the noise at 2.2 V is to measure a cube at a voltage slightly below, to be sure that there is no luminescence at that point, and then use it as dark signal. In this regard, 1.9 V is chosen to measure a cube. Figure 55 shows the spectrum after the subtraction.

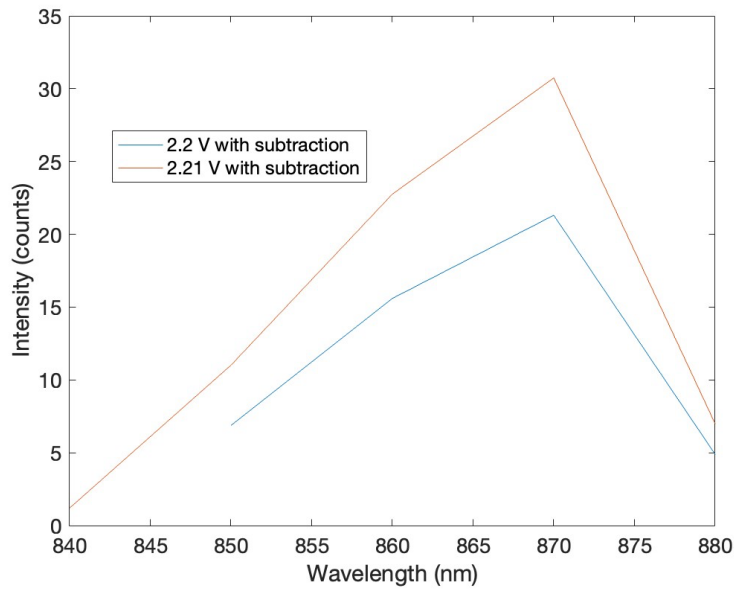


Figure 55. Intensity of the GaAs subcell at 2.2 V and 2.21 V under illumination using the spectrum at 1.9 V as dark to be subtracted.

Looking at Figure 55, the intensity of the signal at 2.2 V and 2.21 V, after a subtraction of a cube measured at 1.9 V, appears like luminescence. Though, the signal is very low.

The same method can be applied to a couple of voltages at a slightly higher value, where the luminescence should be more intense. Since we want to exploit the luminescence at voltages lower than 2.3 V, which should be closer to the maximum power point, 2.25 V and 2.26 V were chosen for this purpose. Figure 56 shows the result of the computation.

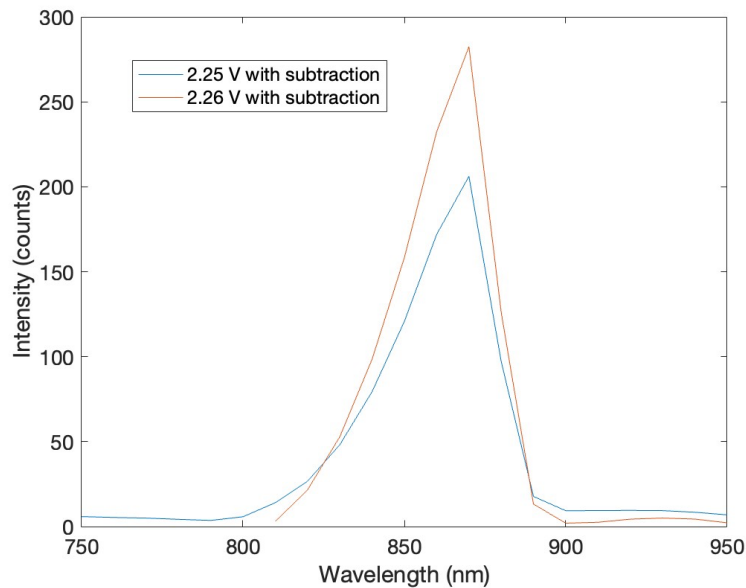


Figure 56. Intensity of the GaAs subcell at 2.25 V and 2.26 V under illumination using the spectrum at 1.9 V as dark to be subtracted.

In this case, the intensity of the signal looks clearly as it is luminescence from GaAs. Indeed, the curve is more like the spectra of luminescence showed before, and from the peak of intensity the material can be identified.

Finally, from the spectral information, the transport efficiency can be calculated. As stated before, writing the reciprocity relation as a function of the luminescence signal, it can be computed as

$$f_t(x, y) = \frac{\delta \ln(\phi_{em}(x, y))}{q\delta V_T/kT} \quad (19)$$

Substituting the peak values of luminescence for the signal at 2.21 V and 2.22 V, which are 30.73 and 21.30 respectively, we find:

$$f_t(x, y) = \frac{\ln(30.73) - \ln(21.30)}{q\delta V_T/kT} = 0.88$$

While for the signal at 2.25 V and 2.26 V we find

$$f_t(x, y) = \frac{\ln(282.44) - \ln(206.15)}{q\delta V_T/kT} = 0.80$$

Nevertheless, despite from the spectral information it is possible to do a manual integration and reconstruct the image of luminescence and therefore compute the map of luminescence, in this case the result concerning the spatial information is not behaving as expected. In fact, even trying to focus on a specific area and integrating only along the wavelength range that gives a significant value for the luminescence, the map shows some negative values. The issue comes in the code when we compute the voltage difference. Indeed, both the internal voltage computed have positive values, but in some points the image at 2.21 V has an internal voltage lower than the one at 2.2 V. The same happens for the couple 2.25-2.26 V. A solution could be taking a cube of luminescence with a lower wavelength step, so that there are more points to do a more accurate integration.

Once we found these two new points for the bottom subcell, they can be substituted in the plot of the surface average f_T as a function of the voltage. The result is shown in Figure 57.

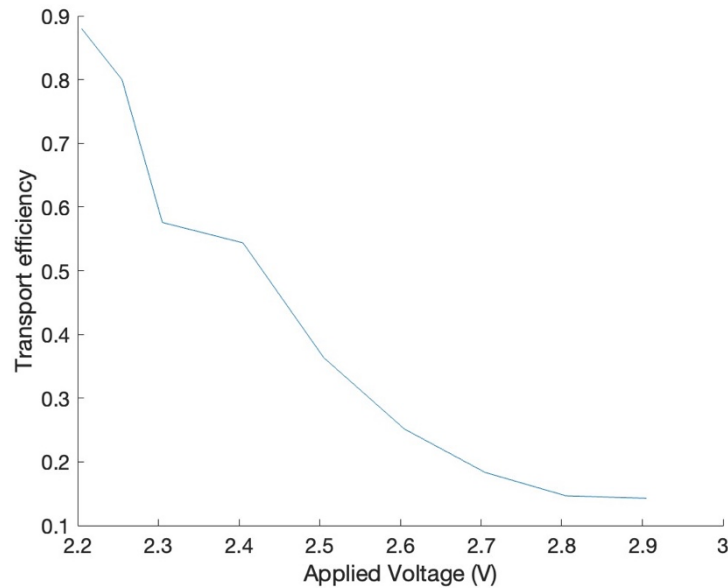


Figure 57. Surface average transport efficiency of the bottom subcell under illumination with the two points found subtracting the background at 1.9 V.

The same method can be applied to the other points for the bottom subcell, and to the top subcell as well, to see what changes in the plot.

7. Conclusions

The principles of electroluminescence and photoluminescence have been thoroughly analyzed in this work. Through luminescence measurements of the spectrum, it was possible to extract and analyze various information about a solar cell: intensity of luminescence, quasi-Fermi level splitting, temperature accuracy, absorptivity (it can be approximated to a value and compared to the EQE, when it is given). The spectral information was complemented with spatial data thanks to the imaging system of the hyperspectral, which reconstructs images of the cell, to have map of luminescence.

In particular, taking advantage of the reciprocity relation, electroluminescence measurements were used to compute transport efficiency. These methods were applied to both single-junction and multi-junction devices, demonstrating the validity of the approach and the capability to obtain map of transport efficiency and its behavior as a function of the increasing voltage.

Specifically, measurements under dark conditions provided a good agreement with results found in the literature. However, when the junction was illuminated, the results became less accurate due to background noise that is independent of the cell itself. Nevertheless, a methodology to reduce the background and utilize spectral information to average the transport efficiency was tested. This approach involves subtracting from the luminescence spectrum at a given voltage, a spectrum measured at a value where there is no effect of luminescence, thus isolating the background effect.

This method was tested under a single condition, and further research is needed to improve it and to explore how spatial information can be extracted. Additionally, for transport efficiency measurements using a light source, only the top subcell was illuminated in this study. However, illuminating the lower cell is also possible, and future studies will investigate this as well as the simultaneous illumination of both cells.

Beyond the results and their potential improvements, it is important to highlight that:

- These measurements were conducted on multi-junction cells, isolating the individual subcells. This demonstrates that *a tandem device can be decomposed and the features of the subcells can be extracted through luminescence measurements*. Once we get the parameters of the single subcells, simulation tools can be also used to simulate the behavior of the cell and make comparisons.

- This technique proves to be rapid (it takes approximately one minute to measure an image, while measuring a spectrum range from 5 to 30 minutes depending on the wavelength step and exposure time) and provides high-resolution results (on the micrometer scale), making it a *straightforward method to replicate*.
- Different illumination intensities and different voltages can be applied to the cell, making the method suitable to *analyze the cell in different conditions, close to real operation*
- Despite the issues related to the background still being present, the strategies used to reduce it represent a good *starting point for developing a new method* to obtain results minimally influenced by it

In the following years, as tandem devices are expected to dominate the market, the understanding of these techniques will be fundamental. New fabrication steps, new materials, new aging mechanisms will bring to the necessity of advanced characterization methods and data analysis, and luminescence will be the one of the starting points.

Appendix

A. Lambert's cosine law

Lambert's cosine law states that the amount of radiant or luminous intensity seen from a perfectly diffuse reflecting surface or ideal diffuse emitter is proportional to the cosine of the angle θ between the observer's view and the perpendicular to the surface and it is expressed as $I = I_0 \cos(\theta)$.

The scenario for a Lambertian surface is depicted in Figure 58. The circle is divided into wedges which represent a solid angle $d\Omega$ of arbitrary size. For a Lambertian surface, the number of photons emitted per second into each wedge is proportional to the wedge's area.

The wedge's length is given by the diameter of the circle multiplied by $\cos(\theta)$. Photon emission reaches the highest value along the surface normal, while it decreases to zero as θ approaches 90° . Mathematically, the radiance along the normal is $I \cdot \text{photons} \cdot (\text{s} \cdot \text{m}^2 \cdot \text{sr})$. The number of photons emitted per second into a vertical wedge is $I d\Omega dA$, while the number of photons emitted into a wedge at θ is $I \cos(\theta) d\Omega dA$.

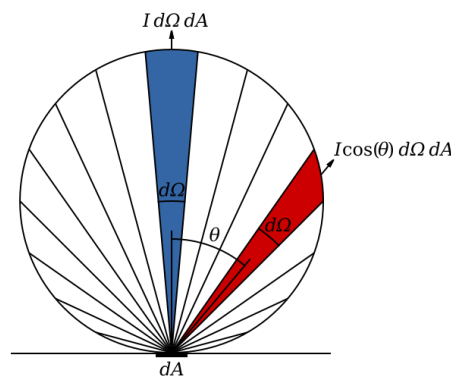


Figure 58. Emission rate (photons/s) in a normal and off-normal direction. The number of photons/sec directed into any wedge is proportional to the area of the wedge.

Credit of the image: https://en.wikipedia.org/wiki/Lambert%27s_cosine_law

B. Measurements on InGaP single junction

For completeness, measurements on InGaP single junction solar cell are also reported. In this case, only electroluminescence measurements have been done, taking into account that also photoluminescence experiments are possible. The setup used is the same as the GaAs single junction cell, except from the objective (in this case, a handmade objective with a lower magnification has been used).

B.1 Dark IV curve

Figure 59 shows the dark IV curve of the cell in logarithmic scale.

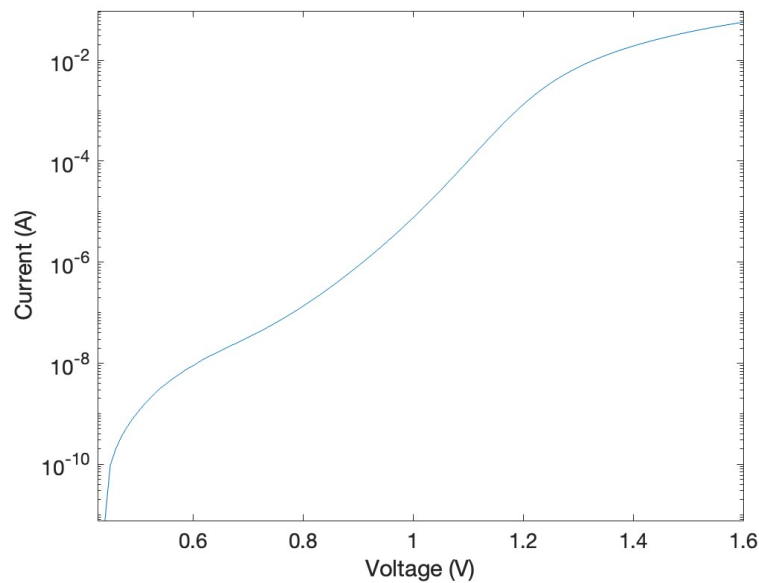


Figure 59. Dark IV curve of the cell.

Looking at the dark IV curve, no particular issues are visible. The effect of series resistance appears around 1.3 V.

B.2 Quasi-Fermi level splitting

The qfls is estimated fitting the Generalized Planck law with an electroluminescence spectrum of the cell measured at 1.3 V. Figure 60 shows the result of the estimation.

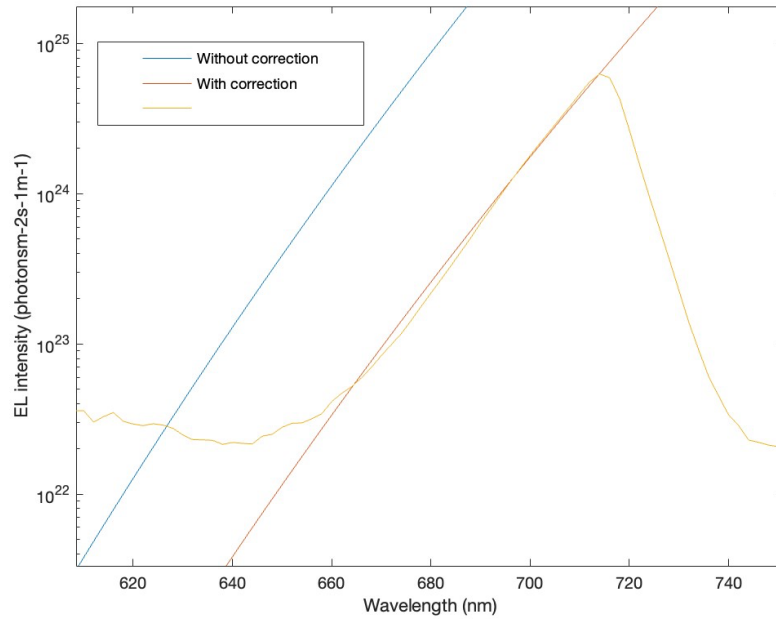


Figure 60. Fit of the Generalized Planck law for the cell with the electroluminescence spectrum measured at $V=1.3$ V. The blue curve is the Generalized Planck law plotted with the initial assumptions ($A=0.74$, $V=1.3$ V, $T=297.15$), the red curve is plotted with the same assumptions for A and T , changing the voltage. A fit with the spectrum is found for $V=1.21$ V.

The blue curve is the Generalized Planck law plotted with the initial assumptions:

- $A \approx 74\%$
- $V=1.3$ V
- $T=297$ K (the temperature measured in the lab was lower, about 293 K; however, it has been increased to adjust the slope of the curve, considering that the temperature of the cell can increase during measurements)

The yellow curve is the fit found with the same conditions for A and T , adjusting the voltage. The fit is obtained for $V=1.21$ V, so there is an uncertainty of 90 mV, which is quite high compared to the ones measured for the GaAs cell. However, it has to be taken into account that the objective used to take this measure is not the Nikon 20x used before, but a handmade one, so there could be differences in the accuracy.

B.3 Images of electroluminescence

Electroluminescence is measured in dark conditions at the voltage 1.2 V, 1.3 V, 1.5 V. Results are shown in Figure 61.

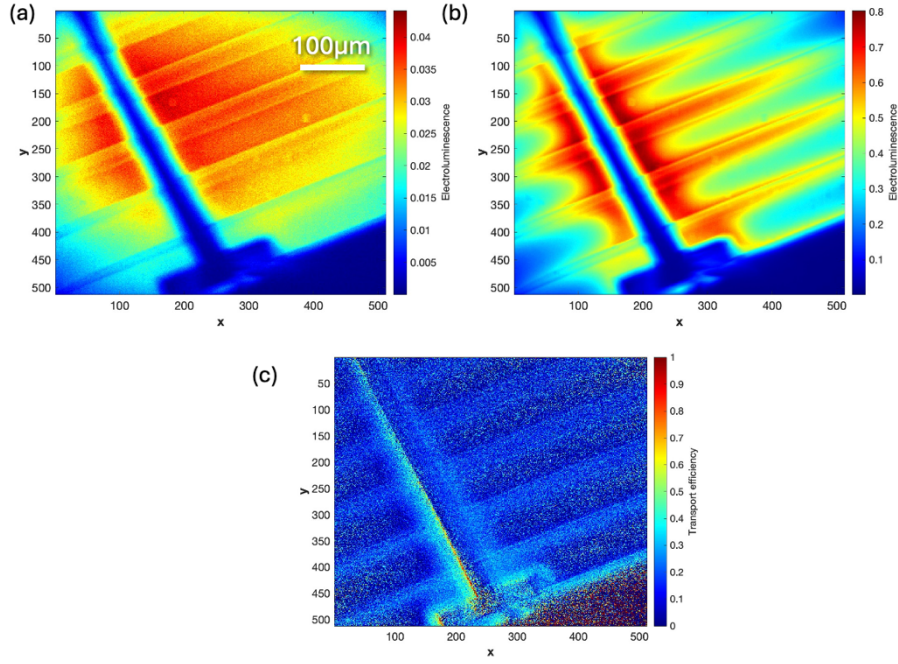


Figure 61. Maps of electroluminescence of the cell at $V=1.2$ V (a) V, $V=1.3$ V (b) and $V=1.5$ V (c).

From the images of luminescence showed above, no particular issues are found in the cell. The behavior is the same described for the GaAs cell.

B.4 Images of transport efficiency

From the images of electroluminescence measured before, it has been computed. Figure 62 shows the maps of the transport efficiency at the different couples of voltages.

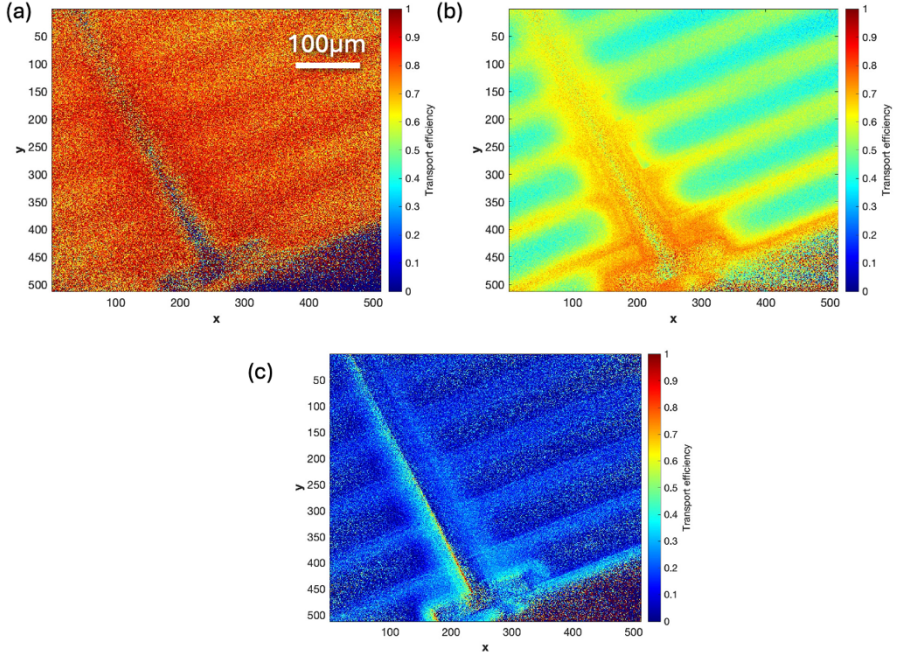


Figure 62. Maps of transport efficiency of the cell at $V=1.2-1.21$ V (a) V, $V=1.3-1.31$ V (b) and $V=1.5-1.51$ V (c).

At low voltages, the transport efficiency is high and close to 1, and it reaches the highest value in proximity of the contacts and the fingers, while it is lower in the other areas. Increasing the voltage, it starts to decrease, reaching almost 0 at higher voltages, where there is an effect of the series resistances.

In addition to the map, averaging over the surface area of the cell, the behavior of the transport efficiency as a function of the voltage can be also plotted. Figure 63 shows the result of the computation, which confirms what we already see from the map.

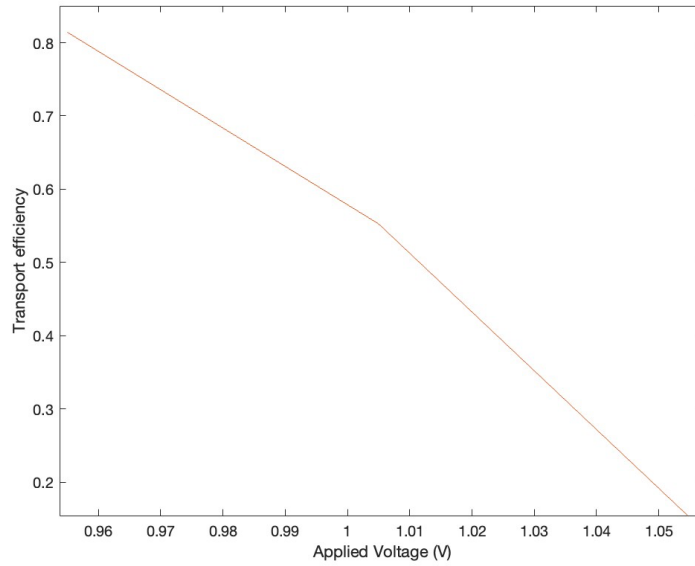


Figure 63. Surface average transport efficiency of the cell as a function of the applied voltage.

References

- [1] Urbina, Antonio. "Sustainability of photovoltaic technologies in future net-zero emissions scenarios." *Progress in Photovoltaics: Research and Applications* 31.12 (2023): 1255-1269.
- [2] Green, Martin A., et al. "Solar cell efficiency tables (version 63)." *Prog Photovolt Res Appl.* 2024; 32(1): 3-13.
- [3] Płaczek-Popko, E. (2017). Top PV market solar cells 2016. *Opto-Electronics Review*, 25(2), 55-64.
- [4] Horowitz, K. A., Remo, T. W., Smith, B., & Ptak, A. J. (2018). *A techno-economic analysis and cost reduction roadmap for III-V solar cells* (No. NREL/TP-6A20-72103). National Renewable Energy Lab.(NREL), Golden, CO (United States).
- [5] Shockley, W., & Queisser, H. (2018). Detailed balance limit of efficiency of p–n junction solar cells. In *Renewable energy* (pp. Vol2 35-Vol2 54). Routledge.
- [6] De Vos, A. (1980). Detailed balance limit of the efficiency of tandem solar cells. *Journal of physics D: Applied physics*, 13(5), 839.
- [7] Kim, S., Hoang, V. Q., & Bark, C. W. (2021). Silicon-based technologies for flexible photovoltaic (Pv) devices: From basic mechanism to manufacturing technologies. *Nanomaterials*, 11(11), 2944.
- [8] Zhang, H., & Park, N. G. (2023). Progress and issues in pin type perovskite solar cells. *DeCarbon*, 100025.
- [9] C.B.Honsberg and S.G.Bowden, "Quantum efficiency" page on www.pveducation.org, 2019.
- [10] Ikeri, H. I., Onyia, A. I., & Asogwa, P. U. (2019). Investigation of optical characteristics of semiconductor quantum dots for multi junction solar cells applications. *International Journal of Scientific & Technology Research*, 8(10), 3531-3535.
- [11] Wurfel, P. (1982). The chemical potential of radiation. *Journal of Physics C: Solid State Physics*, 15(18), 3967.
- [12] Rau, U. (2007). Reciprocity relation between photovoltaic quantum efficiency and electroluminescent emission of solar cells. *Physical Review B—Condensed Matter and Materials Physics*, 76(8), 085303.
- [13] Wong, J., & Green, M. A. (2012). From junction to terminal: Extended reciprocity relations in solar cell operation. *Physical Review B—Condensed Matter and Materials Physics*, 85(23), 235205.
- [14] Delamarre, A., Lombez, L., Watanabe, K., Sugiyama, M., Nakano, Y., & Guillemoles, J. F. (2016). Experimental demonstration of optically determined solar cell current transport efficiency map. *IEEE Journal of Photovoltaics*, 6(2), 528-531.
- [15] Xu, H., Delamarre, A., Yu Jeco, B. M. F., Johnson, H., Watanabe, K., Okada, Y., ... & Sugiyama, M. (2019). Current transport efficiency analysis of multijunction solar cells by luminescence imaging. *Progress in Photovoltaics: Research and Applications*, 27(10), 835-843.

- [16] Delamarre, A., Lombez, L., & Guillemoles, J. F. (2012). Characterization of solar cells using electroluminescence and photoluminescence hyperspectral images. *Journal of Photonics for Energy*, 2(1), 027004-027004.
- [17] Delamarre, A. (2013). Development of luminescence based characterization methods for solar cells.
- [18] Siebentritt, S., Rau, U., Gharabeiki, S., Weiss, T. P., Prot, A., Wang, T., ... & Singh, A. (2022). Photoluminescence assessment of materials for solar cell absorbers. *Faraday discussions*, 239, 112-129.
- [19] Kirchartz, T., Rau, U., Hermle, M., Bett, A. W., Helbig, A., & Werner, J. H. (2008). Internal voltages in GaInP/GaInAs/Ge multijunction solar cells determined by electroluminescence measurements. *Applied Physics Letters*, 92(12).
- [20] Roensch, S., Hoheisel, R., Dimroth, F., & Bett, A. W. (2011). Subcell IV characteristic analysis of GaInP/GaInAs/Ge solar cells using electroluminescence measurements. *Applied Physics Letters*, 98(25).
- [21] Helbig, A., Kirchartz, T., Schaeffler, R., Werner, J. H., & Rau, U. (2010). Quantitative electroluminescence analysis of resistive losses in Cu (In, Ga) Se₂ thin-film modules. *Solar Energy Materials and Solar Cells*, 94(6), 979-984.